ADVANCED FUNCTIONAL MATERIALS
www.afm-journal.de

www.MaterialsViews.com

Hydrogen Incorporation in III-N-V Semiconductors: From Macroscopic to Nanometer Control of the Materials' Physical Properties

Rinaldo Trotta, Antonio Polimeni, and Mario Capizzi*

The effects of hydrogen incorporation in dilute nitride semiconductors, specifically $GaAs_{1-x}N_x$, are discussed. The remarkable consequences of hydrogen irradiation include tuneable and reversible changes in the electronic, optical, structural, and electrical properties of these materials. The highly trapping-limited diffusion of H atoms in dilute nitrides results in the formation of extremely sharp heterointerfaces between H-containing and H-free regions of the crystals. This, in turn, offers an unprecedented possibility to tailor the physical properties of a semiconductor chip in its growth plane with nanometer precision. A number of examples are presented and discussed.

1. Introduction

The capability to modify the physical properties of elemental and compound semiconductors through deliberate incorporation of foreign atoms into the crystal has led to the birth of modern electronics and optoelectronics. Improved performance and multifunctionality of devices have paralleled the progress achieved in the synthesis and engineering of new materials and in the control and modification of their physical properties at small scale lengths. Recently, there has been much interest in the science and applications of highly mismatched alloys, in which small and highly electronegative isovalent impurity atoms are included on the anion sublattice of a III-V compound semiconductor (e.g., GaAs and GaP).[1–3] A well-known example is $GaAs_{1-x}N_x$, where small percentages of nitrogen atoms ($x \approx 1\%$) dramatically perturb the electronic properties of the host crystal, leading to a counterintuitive and large decrease of the bandgap (see **Figure 1**a),[4–7] a non-monotonic variation of the electron effective mass[8–14] and gyromagnetic factor,[15–18] and a softened response to external perturbations, such as hydrostatic pressure[19–25] and temperature.[26–29] All these effects are attributed to the formation of N-related localized states that are resonant with (or close to) the extended states of the conduction band (CB) of GaAs.[4–6,23] The quantum interaction between these two sets of states leads to a distortion of the energy-wavevector dispersion curve and to the formation of a fully developed energy gap in the CB of the host crystal, as shown in Figure 1b.[5,30] This provides not only a parameter for tuning the bandgap energy down to the wavelength region of interest for telecommunications and expanding the range of frequencies exploitable for solar cells,[31,32] but it is also a means for modifying the effective mass and group velocity of conduction electrons with potential for novel electronic devices in the terahertz region.[33,34]

Another important feature that makes dilute nitrides an intriguing material system is the surprising behavior that these semiconductors exhibit after irradiation with hydrogen. It was discovered that hydrogen incorporation modifies the bandgap, E_g, of $GaAs_{1-x}N_x$,[35–37] $In_yGa_{1-y}As_{1-x}N_x$,[38,39] and $GaP_{1-x}N_x$,[40] leading to a recovery of the E_g value of the N-free host; see low-temperature photoluminescence (PL) spectra in **Figure 2**. The bandgap tuning is accompanied by a H-induced variation of the electron effective mass[8,12] and gyromagnetic factor,[15] which clearly indicates that the entire band structure of $GaAs_{1-x}N_x$ is profoundly affected by H. Furthermore, even the structural characteristics of H-irradiated $GaAs_{1-x}N_x$ undergo major modifications. A reversal of strain from tensile to compressive[37,41–44] and an effective re-establishment of local ordering, as found by X-ray absorption fine structure measurements[45] and optical emission spectra,[46] were observed.

Here, we review the intense experimental and theoretical research that these findings have triggered. We focus on the unique capability to spatially control the H–N interaction in $GaAs_{1-x}N_x$ and the resulting materials' physical properties. In particular, by means of a masked-hydrogenation approach, we show that the bandgap energy can be controlled in the plane of the alloy down to the nanometer scale length, thus making way for the possible realization of a novel class of size- and site-controlled semiconductor nanostructures. Using the same methodology, we also obtain control of the polarization state of the light emitted by strain-engineered planar microstructures. Finally, the effects of H incorporation on the refractive index and electrical resistance of $GaAs_{1-x}N_x$ are reviewed.

Dr. R. Trotta, Prof. A. Polimeni, Prof. M. Capizzi
Dipartimento di Fisica, Sapienza Università di Roma
Piazzale A. Moro 2, 00185 Roma, Italy
E-mail: antonio.polimeni@roma1.infn.it

DOI: 10.1002/adfm.201102053

2. Experimental and Theoretical Details

Here we report some details about the experimental and theoretical techniques mentioned in this article. We refer the reader to specific papers for a more complete description.

2.1. Samples

All $GaAs_{1-x}N_x$ samples were grown at 500 °C by molecular beam epitaxy on top of a 500 nm-thick GaAs buffer layer deposited at 600 °C on a (001) semi-insulating GaAs substrate. Different nitrogen concentrations and $GaAs_{1-x}N_x$ layer thicknesses were employed, depending on the specific application.

2.2. Hydrogen Irradiation

All samples were H-irradiated by a Kaufman source (100 eV ion beam energy) with the samples held at a fixed temperature T_H. T_H values varied between 200 °C and 350 °C. Typical ion current densities are few tens of μA cm^{-2}.[38] For specific analytical techniques sensitive to ion mass, such as secondary ion mass spectrometry,[47] nuclear reaction analysis,[42] and far-infrared absorption spectroscopy,[48] deuterium was used in place of hydrogen. We point out that D and H have the same consequences on the physical properties of dilute nitrides.[44]

For in-plane engineering of the physical properties of the samples, the specimen surface was covered with titanium patterns that had thicknesses equal to about 50 nm and different shapes and sizes. Ti was chosen because of its opacity to hydrogen and ease of removal from GaAs-like surfaces by hydrofluoric acid. The Ti patterns were fabricated using high-voltage (100 kV) electron-beam lithography and a lift-off technique.[49]

2.3. Structural Characterization

For secondary ion mass spectrometry measurements (SIMS), an E_{Cs} = 1 keV Cs^+ primary beam at oblique incidence (55°) was used in a CAMECA Sc-Ultra mass spectrometer, where $^2H^-$ and $^{75}As^-$ negative secondary ions were collected with a depth resolution of 2–3 nm per decade.[50] The sputtering time was converted to an in-depth scale by measuring the obtained crater depths with a mechanical stylus profilometer with few nanometer resolution. Measurements of the lattice parameter were carried out using a Philips X'Pert PRO MRD diffractometer. A 1.2 MeV D^+ beam delivered by the CN accelerator at the Laboratori Nazionali di Legnaro (Italy) was used to perform nuclear reaction analysis with the $^2H(d,p)^3H$ and the $^{14}N(d,\alpha)^{12}C$ reactions.[42]

2.4. Optical Characterization

The electronic properties of the samples were investigated using continuous-wave photoluminescence (PL) with a vanadate:Nd laser (λ = 532 nm) for excitation. For conventional measurements on untreated samples, a PL set-up with a laser spot diameter, *s*, of about 200 μm was employed. For micro-photoluminescence (μ-PL) measurements addressing the properties of single heterostructures, we used a microscope objective

Rinaldo Trotta received his PhD in Materials Science in 2008 at the Dipartimento di Fisica, Sapienza Università di Roma. Since 2010, he has been a postdoctoral research associate at the Institute for Integrative Nanosciences in Dresden (Germany), where he is presently working on the fundamental properties of quantum dots for quantum information applications.

Antonio Polimeni is an Associate Professor in Experimental Physics at the Dipartimento di Fisica, Sapienza Università di Roma. He received his PhD in Physics in 1996 and was a postdoctoral research associate at the School of Physics and Astronomy, Nottingham University (UK) from 1997 to 1999. His research focuses on the optical and transport properties of semiconductor materials and nanostructures.

Mario Capizzi is a Full Professor of Condensed Matter Physics in the Physics Department at the Sapienza University of Rome, where he received his Diploma in Physics in 1968. He was visiting researcher at ETH (Zurich, 1969), ENS (Paris, 1974–75), and Bell Laboratories-Murray Hill (NJ, USA, 1977–1979). His research focuses on the optical properties of solids (Si, Ge, III-V alloys, and high T_c superconductors) at low and high excitations (electron-hole droplets and plasmas) and high doping (metal-insulator transition). Recently, he has investigated the effects of hydrogen irradiation on dilute nitrides.

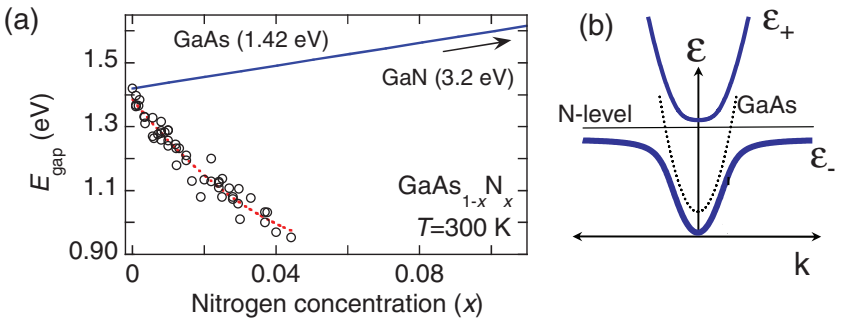

Figure 1. a) Dependence on N concentration of the bandgap energy (E_{gap}) of $GaAs_{1-x}N_x$ at room temperature (open circles). The solid line shows the E_{gap} values expected within a conventional virtual crystal approximation, which is not applicable here. b) Sketch of the energy-wavevector dispersion curve (thick solid line) assuming a simple two-level interaction between a single N level (horizontal solid line) and the parabolic conduction band (CB) of GaAs (dotted line). Note the CB splitting in ε_- and ε_+ bands, with ε_- being the new conduction band minimum.

(100× and 0.8 numerical aperture (NA)) resulting in $s \approx 1$ μm. In both cases, the luminescence was spectrally analyzed by a 0.75 m monochromator and detected by a N-cooled charge-coupled device (CCD) detector or an InGaAs array detector. In magneto-PL experiments, the samples were mounted in a non-magnetic Ti- and carbon-body insert, which was then placed in the bore of a 30 T water-cooled Bitter magnet. The insert was composed of a 40× microscope objective (with NA = 0.65 and spatial resolution ≈1 μm), a three-axis piezoelectric nanopositioner, and a sample holder. The PL signal was excited by a 532 nm laser and spectrally analyzed and detected by a 0.30 m monochromator coupled to a Si CCD detector. Throughout the measurements, the sample was kept at a temperature $T \approx 4.2$ K in a liquid He-bath cryostat.[49] Polarization-resolved PL was performed by using a liquid crystal variable retarder and a fixed linear polarizer (analyzer) in order to disregard the response to polarization of the optical set-up.[51]

For time-resolved μ-PL measurements a dye laser ($\lambda = 600$ nm) pumped by the second harmonic of a neodymium-doped yttrium aluminium garnet (Nd:YAG) pulsed laser was used for excitation; the pulse duration was 5 ps and the repetition rate was 76 MHz. For light collection, a confocal microscope configuration was used with two different infinity objectives. The μ-PL signal was then focused onto a multimode optical fiber and dispersed by a single grating spectrometer with 25 cm focal length. It was then detected by an $In_{1-x}Al_xAs/In_{1-x}Ga_xAs$ photomultiplier followed by a photon counting apparatus for PL measurements and a time-correlated single-photon counting setup providing an experimental time resolution of 200 ps for time-resolved spectra.

2.5. Theoretical Models

For hydrogen diffusion modelling, finite-element calculations were employed to solve the set of partial differential equations that govern the diffusion of hydrogen in $GaAs_{1-x}N_x$, as it will be described in the Section 3.2. For strain calculations, we used the equilibrium elasticity theory employing a finite-element method in the framework of thermoelasticity. The elasticity parameters entering into calculations were fixed so as to reproduce the experimental values of the strain found in bulk samples.[51,52]

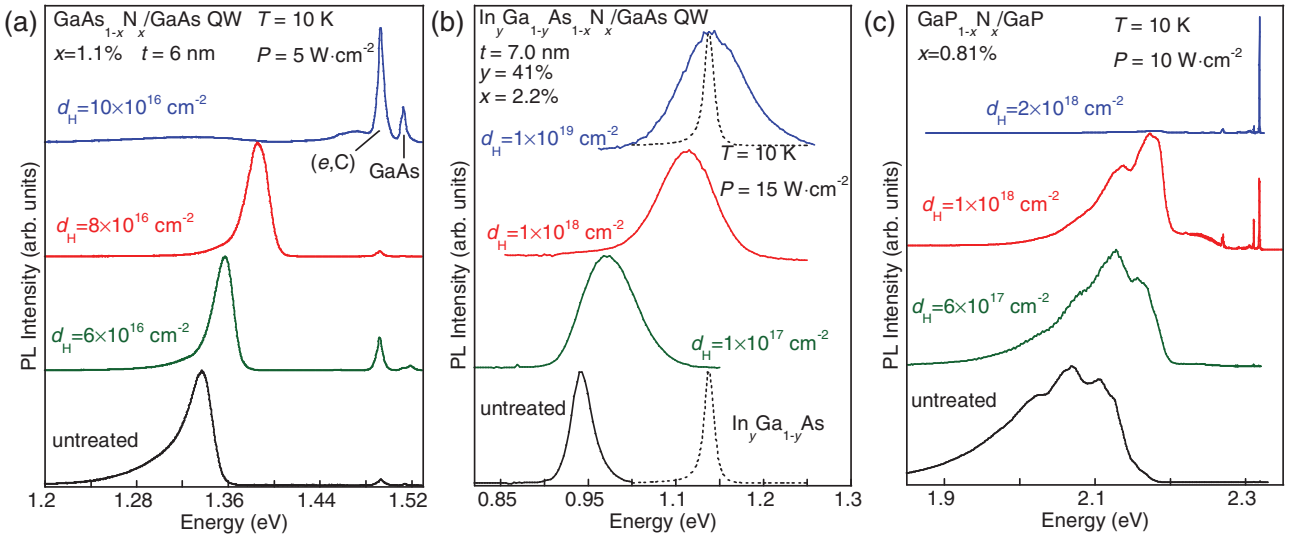

Figure 2. PL spectra at $T = 10$ K of different dilute nitride systems treated with increasing hydrogen doses d_H. a) $GaAs_{1-x}N_x/GaAs$ quantum well with thickness $t = 6$ nm. b) $In_yGa_{1-y}As_{1-x}N_x/GaAs$ quantum well with $t = 7$ nm. The dashed line is the PL spectrum of the N-free $In_yGa_{1-y}As/GaAs$ quantum well. c) $GaP_{1-x}N_x/GaP$ epilayer with a thickness equal to 250 nm. The top most spectrum coincides with that of a sample with an N effective concentration <0.01%.

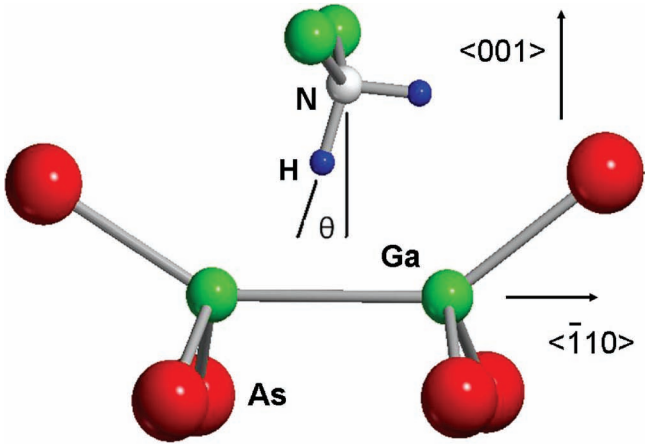

Figure 3. The relaxed C_{1h} defect in $GaAs_{1-x}N_x$. The angle θ is the canting angle of the N-passivating C_{1h} center. Reproduced with permission.[64] Copyright 2010, American Physical Society.

3. Hydrogen Diffusion in $GaAs_{1-x}N_x$

3.1. How Many Hydrogen Atoms Per N Atom?

The answer to this question is a key point for the modelling and prediction of the kinetics of hydrogen in dilute nitrides and, of course, it is strictly related to the geometry and stoichiometry of the complex responsible for the electronic passivation of N atoms. Early theoretical calculations suggested that nitrogen-stabilized H_2^*(N) structures with one H atom at a bond-centered site and a second H at an antibonding site with respect to the N atom along the same Ga-N <111> axis would account for the bandgap shifts caused by H.[53–58] However, these H_2^*(N) complexes were inconsistent with the vibrational properties of hydrogenated $GaAs_{1-x}N_x$. In fact, infrared (IR) absorption studies of $GaAs_{1-x}N_x$ epilayers treated with both hydrogen and deuterium revealed that the defect causing the passivation of the electronic activity of N has two inequivalent, weakly coupled N–H stretching modes.[48,59] Therefore, alternative H–N–H structures with C_{2v} symmetry or with a canted C_{1h} geometry (**Figure 3**) have been proposed.[60–63] The observed vibrational properties are most consistent with the canted H–N–H structure with C_{1h} symmetry.[64] Additionally, this C_{1h} complex accounted for the X-ray absorption near-edge structure of N atoms performed in hydrogenated $GaAs_{1-x}N_x$ using a synchrotron radiation source[62] and, to date, it is the most likely complex responsible for nitrogen passivation.

We next summarize the experimental evidence that discloses the presence of an additional hydrogen atom in the complex depicted in Figure 3. As it will be shown in the following, this extra H atom plays a great role in determining the lattice properties of hydrogenated $GaAs_{1-x}N_x$. **Figure 4**a shows the concentration of deuterium atoms in a $GaAs_{1-x}N_x$ sample (x = 1.22%, thickness t = 220 nm) subjected to different post-growth treatments. The concentration was determined by exploiting the by-products of different controlled nuclear reactions, as described in detail elsewhere.[42] The bottom-most line refers to the untreated sample, while the upward displaced lines refer to post-growth treated samples. The corresponding lines in panels (b,c) show the PL spectra and X-ray diffraction rocking curves of the same samples, respectively. All measurements were performed at room temperature. In particular for PL, this experimental conditions allow one to avoid the contribution from localized states that may affect the spectrum lineshape,[26] thus rendering a reliable estimate of the bandgap energy difficult. After deuterium irradiation, all N atoms are fully passivated, as evident from the PL spectrum in panel (b) and the ratio between D and N atoms is equal to three (see panel (a)). At the same time, the tensile strain of $GaAs_{1-x}N_x$ becomes compressive as determined by the change in sign of the diffraction angle of the N-containing layer shown in panel (c).[41–42,44] A moderate annealing at 250 °C does not vary the bandgap energy of the deuterated sample (see corresponding PL spectrum in panel (b)) but changes the ratio of D to N atoms from three to two (panel (a)) and makes the N-containing layer lattice-matched to the GaAs substrate (panel (c)). Finally, annealing at high temperature (325 °C) restores the electronic and lattice properties of untreated $GaAs_{1-x}N_x$ in accordance with the small concentration of D atoms left in the crystal (most likely in the interstitial position).

In summary, the interaction of H (or equivalently D) with N leads to the formation of (N–2H)–H complexes where: i) two H atoms bind to a single N atom forming a very stable N–2H complex, which is responsible for the electronic passivation of nitrogen (see Figure 3) and ii) a third H atom is more weakly trapped near passivated N atoms and causes a compressive strain in the $GaAs_{1-x}N_x$ layer (the exact position of this satellite H atom is yet unknown). Careful X-ray diffraction measurements on hydrogenated $GaAs_{1-x}N_x$ samples subjected to different thermal annealings showed that the third H atom is removed from its site at 250 °C with an activation energy equal to 1.77 eV. At the same time, the compressive strain disappears while N atoms are still electronically passivated (namely, the bandgap energy of $GaAs_{1-x}N_x$:H is equal to that of GaAs). A higher activation energy (1.89 eV) instead characterizes the dissociation of the N–2H complexes and the concomitant recovery of the $GaAs_{1-x}N_x$ pristine properties, e.g., bandgap energy value and lattice constant.[41]

3.2. Modelling Hydrogen Diffusion in $GaAs_{1-x}N_x$

We have shown that hydrogen irradiation is an exceptional tool for modifying, on demand, the physical properties of $GaAs_{1-x}N_x$ (and other dilute nitrides), in the first instance the bandgap energy and lattice constant. Other important properties (e.g., refractive index[65] and electrical resistance[66]) can be also controlled, as will be shown in the following. Here, we are primarily interested to establish to what extent the formation of the N-passivating C_{1h} complexes can be spatially controlled.

Figure 5a shows the deuterium profile in different $GaAs_{1-x}N_x$ samples determined by secondary ion mass spectrometry. All samples were deuterated at a temperature T_D = 300 °C. It can be clearly observed that the deuterium forefront becomes sharper as the N concentration increases. In particular, for x > 1% the deuterium concentration falls by a factor 10 within 10 nm. Remarkably, this quantity reaches a value as small or less than 5 nm for a deuteration temperature equal to T_D = 200 °C, as

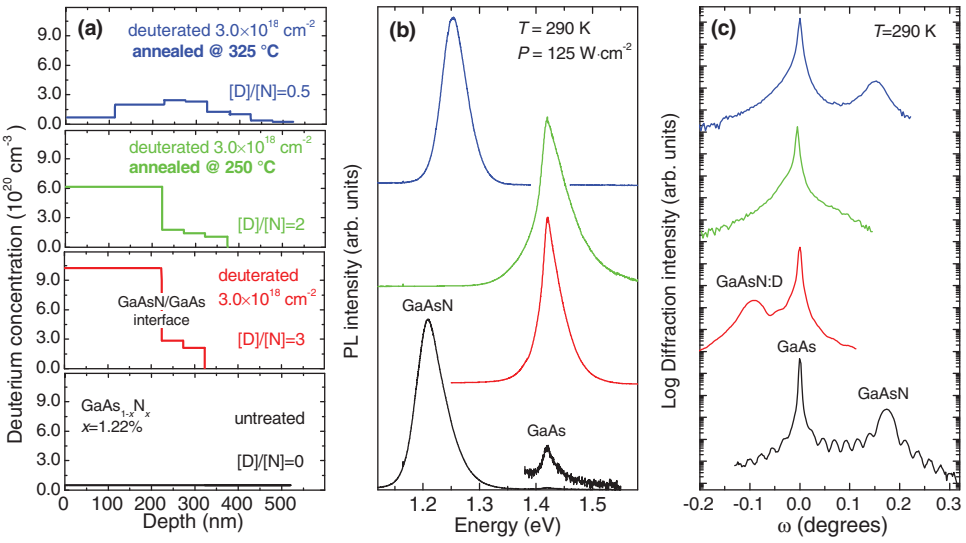

Figure 4. a) Deuterium depth profiles derived from ^{3}He(d,p)^{4}He reaction in a 220 nm-thick $GaAs_{0.9878}N_{0.0122}$ sample before the deuteration process (bottom-most line), at the end of the deuteration process (second line from the bottom), at the end of the 250 °C annealing stage with duration 13 h (third line from the bottom), and at the end of the 325 °C annealing stage with duration 4.7 h (top-most line). Zero on the abscissa axis indicates the sample surface. b) PL spectra at T = 290 K of the samples displayed in panel (a). c) (004) X-ray diffraction rocking curves of the samples shown in panels (a,b).

shown in panel (b) for x = 0.7% along with the predictions of a model developed to take into account the particular formation and dissociation kinetics of the (N–2D)–D complex. This is described in detail in the following. According to the experimental and theoretical results presented so far, we assume that D capture ceases as soon as three D atoms bind to one N atom, resulting in a multiple trapping process.[67] Treating the $GaAs_{1-x}N_x$ epilayer as a semi-infinite medium ($z \geq 0$), we define $n_D(z,t)$ as the concentration of free unbound D atoms and $n_{NiD}(z,t)$ as the concentration of immobile N atoms with i = 0, 1, 2, and 3 bonded D atoms such that the spatially uniform N concentration is $n_N = \Sigma_{i=0,3}\, n_{NiD}(z)$. For $z \geq 0$ and $t \geq 0$, the time (and space for unbound D only) evolution of the involved species is given by

$$\frac{\partial n_D}{\partial t} - D_{dif}\frac{\partial^2 n_D}{\partial z^2} = -k(n_D n_{N0D} + n_D n_{N1D} + n_D n_{N2D}) + \gamma_a n_{N3D} + \gamma_b n_{N2D} + \gamma_c n_{N1D} \quad (1)$$

$$\frac{\partial n_{N0D}}{\partial t} = -kn_D n_{N0D} + \gamma_c n_{N1D} \quad (2)$$

$$\frac{\partial n_{N1D}}{\partial t} = kn_D n_{N0D} - kn_D n_{N1D} - \gamma_c n_{N1D} + \gamma_b n_{N2D} \quad (3)$$

$$\frac{\partial n_{N2D}}{\partial t} = kn_D n_{N1D} - kn_D n_{N2D} - \gamma_b n_{N2D} + \gamma_a n_{N3D} \quad (4)$$

$$\frac{\partial n_{N3D}}{\partial t} = kn_D n_{N2D} - \gamma_a n_{N3D} \quad (5)$$

$\gamma_m = \nu_m \exp(-E_m/k_B T)$ (with m = a,b,c) is the dissociation rate of the particular complex considered,[67] where ν_m is the attempt frequency and E_m is the activation energy for the dissociation. k is the deuterium capture rate coefficient for the different complexes considered[67] and, for simplicity, it is assumed to

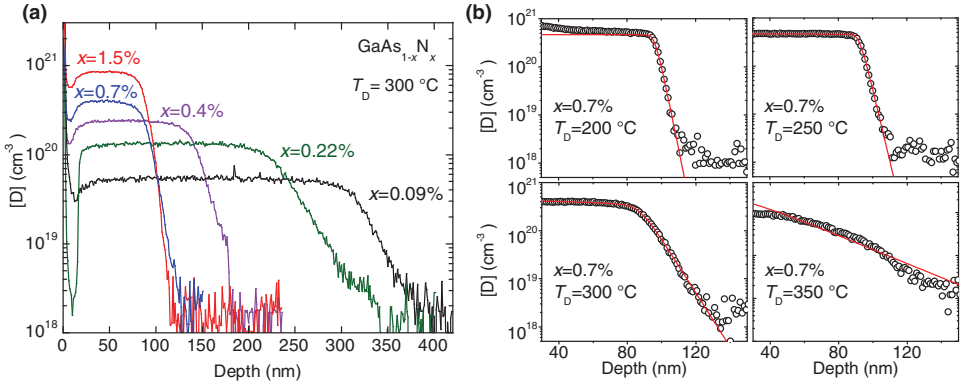

Figure 5. a) SIMS depth profile of deuterium concentration (the origin is set at the sample surface) for $GaAs_{1-x}N_x$ samples with different N concentration x. The sample irradiation temperature was T_D = 300 °C. b) Same as (a) for x = 0.7% and different irradiation temperatures.

be independent of the trapping step. On the right-hand side of Equation (1), the first term represents the capture of one D atom by N atoms with i (= 0,1,2) D atoms already bonded. The second, third, and fourth terms, respectively, account for the thermal release of one D atom from an N–2D–D, an N–2D, and an N–1D complex. As mentioned in Section 3.1, previous experiments disclosed the existence of two steps in the dissolution of N–2D–D complexes.[41–42] In the first step, a D atom is removed leaving an N–2D complex. In the second step the N–2D complex is dissociated by releasing two D's simultaneously, thus leaving an isolated unpassivated N atom. Therefore, the second and third D atom are released with a same activation energy and we will effectively assume $\gamma_a \neq \gamma_b = \gamma_c$. Finally, Equations(2–5) represent the time evolution of the immobile species. The system of five coupled partial differential Equations (1) to (5) is solved numerically with the following initial and boundary conditions: $n_{NiD}(z,0) = 0$ for $(z > 0)$ and $i = 1,2,3$; $n_{N0D}(z,0) = n_N$ for $z > 0$; $n_D(0,t)$ = constant (set by the current of impinging D^+ ions during the experiment); and $n_{N0D}(0,t) = 0$; $n_D(\infty,t) = n_{N1D}(\infty,t) = n_{N2D}(\infty,t) = n_{N3D}(\infty,t) = 0$. Finally, the total deuterium depth profile is given by

$$n_D^{tot}(z) = n_D + \sum_{i=1,3} i n_{NiD}. \quad (6)$$

We obtain a very good agreement between model and experiments, as shown in Figure 5b. A similar agreement has been achieved for all N concentrations considered. During the fitting procedure we fixed the D exposure times to be equal to those used experimentally, the N concentration n_N was equal to the nominal value of the $GaAs_{1-x}N_x$ samples, and $\nu = 90$ THz for both detrapping processes.[37] k and E_m were used as free parameters. In agreement with previous annealing studies,[41] $E_a = (1.75 \pm 0.03)$ eV and $E_b = (2.0 \pm 0.1)$ eV is the only pair of activation energies that consistently fit all the deuterium profiles. Notice that the discrepancy between the model and experimental data for depths <40 nm and $T_D = 200$ °C is due to D accumulation. In fact, D may form stable, albeit weak, bonds to defects differently than N atoms or N complexes, resulting in an increase in D concentration close to the surface at low T.

The steepness and shape of the D trailing edge also reflect the sample optical properties. In particular, in synergy with SIMS, PL can be effectively used to estimate the extent of the D-free $GaAs_{1-x}N_x$ thickness after irradiation. **Figure 6**a shows the SIMS depth profiles of deuterium for an $x = 0.4\%$ sample with a thickness of 180 nm. The sample irradiation temperature was 300 °C and two different D impinging ion doses were employed by using the same ion current but different exposure times. This results in a nearly rigid shift of the D concentration trailing edge. The PL spectra of the two samples (dashed line plus squares for lower dose and dashed line plus circles for higher dose) at 150 K are shown in Figure 6b and that of the untreated $GaAs_{1-x}N_x$ (solid line) is also shown. This relatively high measurement temperature allows the substantial decrease in the contribution of localized states,[26] while retaining a good PL signal-to-noise ratio. Notice that the peak energy of the $GaAs_{1-x}N_x$-related emission is the same in the untreated and in the low-dose irradiated sample (open squares in Figure 6), while the weight of the GaAs-related emission relative to that

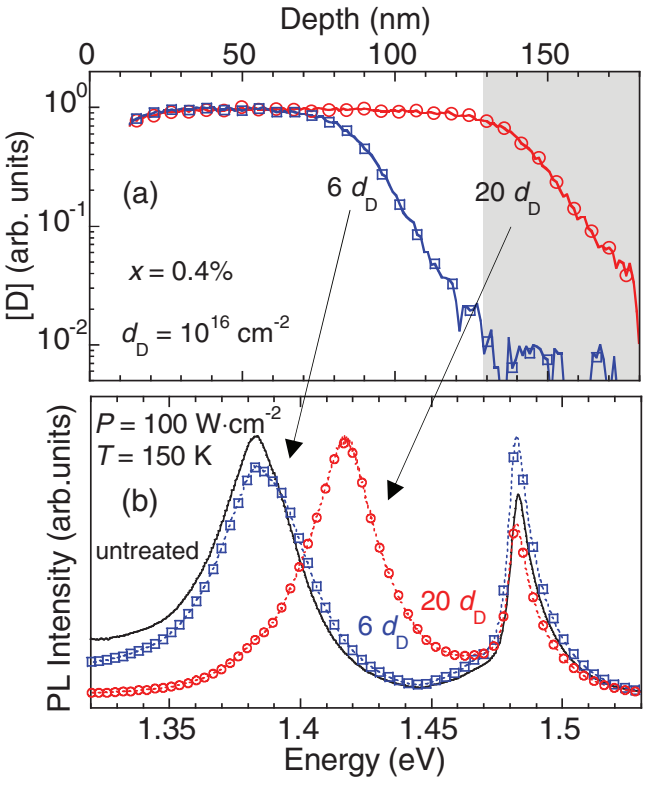

Figure 6. a) SIMS depth profiles of deuterium in a $GaAs_{1-x}N_x$ sample with $x = 0.4\%$ and a thickness equal to 180 nm. The sample irradiation temperature was 300 °C and two different ion impinging doses were used: lower dose (squares, $d_D = 6 \times 10^{16}$ cm^{-2}) and higher dose (circles, $d_D = 2 \times 10^{17}$ cm^{-2}). b) PL spectrum at 150 K of the untreated sample (solid line), of the low-dose deuterated sample (dashed line and squares, $d_D = 6 \times 10^{16}$ cm^{-2}), and of the high-dose deuterated sample (dashed line and circles, $d_D = 2 \times 10^{17}$ cm^{-2}). The SIMS data for the latter two samples are shown in panel (a). The PL bands peaked at ≈1.38 eV correspond to the carrier recombining in deuterium-free $GaAs_{1-x}N_x$. The PL peak at ≈1.48 eV is due to carrier recombination in GaAs or fully passivated $GaAs_{1-x}N_x$ regions. The band at ≈1.42 eV originates from the carrier recombining in the sample region located at the deuterium forefront, where a partial passivation of N atoms occurred (highlighted by the gray region in panel (a)).

of the $GaAs_{1-x}N_x$-related emission is slightly higher in the latter sample. In a PL experiment, carriers relax toward regions of the sample with the lowest bandgap energy before recombining radiatively. Therefore, in the sample deuterated at a lower dose no sizable carrier recombination occurs in the fully or partially deuterated regions closer to the sample surface and almost all luminescence originates from the D-free 50 nm-thick $GaAs_{1-x}N_x$ layer (highlighted by a grey rectangle in Figure 6b) at the $GaAs_{1-x}N_x$/GaAs interface. In the sample irradiated at higher D dose, the low-energy band due to $GaAs_{1-x}N_x$ is blue-shifted by about 40 meV because a partial N passivation occurs at the interface between the $GaAs_{1-x}N_x$ and GaAs buffer layers, where the SIMS shows a sizable D concentration; see panel (a). Consequently, a fine tuning of the effective N concentration in dilute nitrides can be realized, especially in $GaAs_{1-x}N_x$ epilayers with small N concentration and in $GaAs_{1-x}N_x$ (or $In_yGa_{1-y}As_{1-x}N_x$) quantum wells. In these latter heterostructures, one exploits the small thickness of the well (usually a few nanometers) in

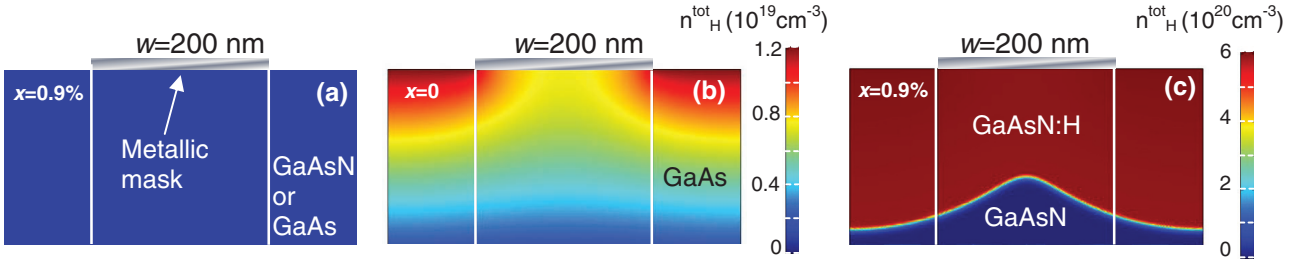

Figure 7. a) Sketch of sample before H irradiation. Post-hydrogenation distribution of the total H atoms as obtained by solving Equations (1–6) in two dimensions and in the presence of a 200 nm wide metallic mask. b) Simulation for $x = 0$ and $T_H = 200$ °C. c) Simulation for $x = 0.9\%$ and $T_H = 200$ °C. The diffusion coefficient (2.0×10^{12} cm^2 s^{-1}) and the time (420 s) used for the calculations are the same in (b) and (c). The total deuterium concentration is shown in a false color scale. Notice the factor 50 difference in the color scale between (b) and (c).

order to quite uniformly vary the density of electronically active N atoms.

3.3. Engineering H Incorporation in $GaAs_{1-x}N_x$

In the previous section we have shown that a tight spatial control of the N–H (or N–D) interaction can be achieved in the crystal growth direction. A most relevant objective of our studies is to extend this control in the sample growth plane at the nanometer scale length. As shown in **Figure 7**a, a titanium mask opaque to hydrogen is deposited on the surface of a $GaAs_{1-x}N_x$ sample and patterned by electron-beam lithography in order to impede H diffusion in well-defined and arbitrarily shaped regions of the sample. The results of a 2D simulation based on Equations (1–6) of H diffusion in samples covered by a 200 nm wide wire are shown in panel (b) for a N-free GaAs layer and in panel (c) for $GaAs_{1-x}N_x$ epilayer with $x = 0.9\%$ and hydrogenated at 200 °C. The boundary and initial conditions used in the calculations were set equal to those used experimentally to obtain the nanostructures described in the following. The sample section displayed in Figure 7 contains the growth axis of the sample and is perpendicular to the metallic wire direction. The colored scale shows the total hydrogen concentration, namely, n_H^{tot}, see Equation (6). From a comparison of Figure 7b,c it is clear that N dramatically modifies the H kinetics in GaAs, altering both the depth and the lineshape of the hydrogen advancing profile. In particular, in the N-free GaAs epilayer, panel (b), a purely Fick-like diffusive motion is found with a H concentration smeared over the forefront. On the other hand, in panel (c) the high density of N traps (2×10^{20} cm^{-3}) in the $GaAs_{0.991}N_{0.009}$ layer turns free diffusion of H into a multiple-trapping process that drastically affects the distribution of H atoms, resulting in a cross-over region between H-free and H-containing $GaAs_{1-x}N_x$ as sharp as few nanometers.

The results reported so far show that the diffusion of H in a medium such as $GaAs_{1-x}N_x$ with such a high trap density can be tightly controlled. This fact, combined with the peculiar effects that H has on the electronic properties of dilute nitrides, renders $GaAs_{1-x}N_x$ an example in solid state physics of a system whose entire physical properties can be modified on demand and at the nanometer scale. This gives us the unprecedented possibility to design desired structures with specific physical properties. We performed a series of simulations of H diffusion in different $GaAs_{1-x}N_x$/GaAs heterostructures ($x = 1\%$), whose surfaces are covered by different Ti masks. **Figure 8** shows the distribution of unpassivated (or electronically active) N atoms following H incorporation. Panel (a) refers to a 200 nm-thick $GaAs_{1-x}N_x$ epilayer covered with a Ti wire that has a width equal to 80 nm. The initial bulk-like layer becomes a thin quantum well with a thickness equal to ≈8 nm. The formation of a quantum wire starting from a 50 nm-thick $GaAs_{1-x}N_x$ epilayer (on which a 50 nm-wide Ti wire has been deposited) is

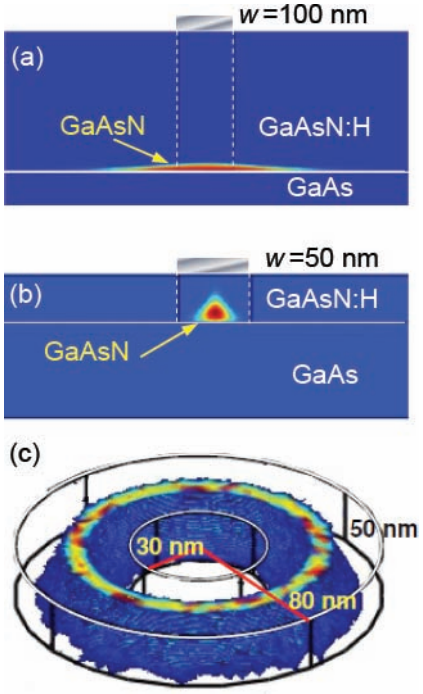

Figure 8. a) Post-hydrogenation distribution of electronically active N-atom density in a $GaAs_{1-x}N_x$ epilayer ($x = 0.9\%$ and $t = 200$ nm) in the presence of a 100 nm-wide Ti wire. The irradiation temperature used for the calculation was 200 °C. b) Post-hydrogenation distribution of electronically active N-atoms in a $GaAs_{1-x}N_x$ epilayer ($x = 0.9\%$ and $t = 50$nm) in the presence of a 50 nm-wide Ti wire. The irradiation temperature used for the calculation was 300 °C. In panels (a) and (b) the wires run perpendicular to the figure plane. d) 3D post-hydrogenation distribution of N-atom density in a $GaAs_{1-x}N_x$ epilayer ($x = 0.9\%$ and $t = 50$ nm) in the presence of a Ti ring. The size of the inner (outer) diameter is 30 (80) nm. The irradiation temperature used for the calculation was 200 °C. Red and blue correspond to maximum and minimum N concentration, respectively.

displayed in panel (b). Finally, Figure 8c shows a 3D simulation of the formation of a quantum ring starting from a 50 nm-thick $GaAs_{1-x}N_x$ epilayer. Since regularly shaped quantum rings are very difficult to obtain by self-assembly techniques based on molecular beam epitaxy,[68] alternative methods, such as the one here reported, would be of particular importance.

4. Fabrication and Characterization of $GaAs_{1-x}N_x$ Nanostructures Based on Tailored Hydrogen Incorporation

4.1. From 3D to 2D

We demonstrate first that quantum confinement can be obtained starting from a bulk sample. In particular, we consider a 200 nm-thick $GaAs_{1-x}N_x$ layer with a nitrogen concentration equal to 0.9%. On top of the N-containing layer, a 50 nm-thick film of titanium is deposited and patterned using electron-beam lithography so as to obtain ensembles of Ti wires with different widths, w.[69,70] The metallic wires were 5 μm apart from each other and 485 nm, 175 nm, and 80 nm wide, as determined by scanning electron microscopy. The patterned sample was hydrogenated at 300 °C. **Figure 9**a–c shows the calculated distribution of unpassivated (or electronically active) N atoms (n_{N0H}) in different $GaAs_{1-x}N_x$ wires. We point out that these H-free N atoms ultimately determine the potential depth to which carriers are

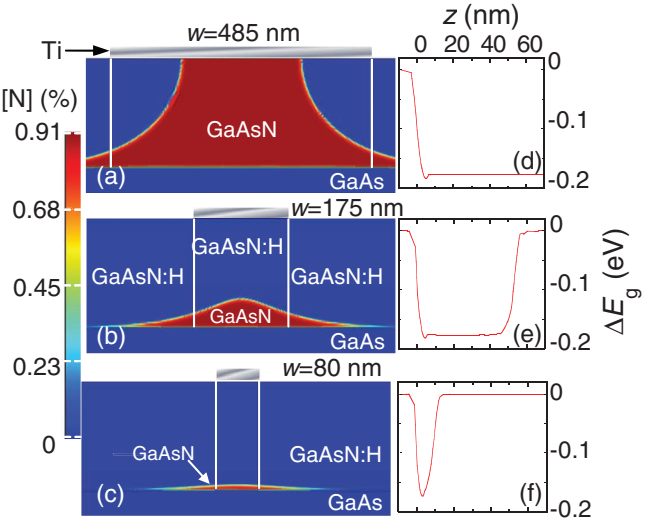

Figure 9. Left panels: Post-hydrogenation distribution of electronically active N atoms in a sample section containing the growth axis. The wires run perpendicular to the figure plane and the Ti wire is sketched as a grey rectangle on the top surface. Panels (a–c) are simulations of the effective N concentration obtained by solving Equations (1–6) for Ti wires deposited on the $GaAs_{1-x}N_x$ surface with widths equal to w = 485 nm, w = 175, and w = 80 nm, respectively. The N atom concentration is shown in a false color scale on the left. Right panels: bandgap energy modulation, ΔE_g, along the vertical symmetry axis of the wires (z runs from the buffer/$GaAs_{1-x}N_x$ interface, z = 0 nm, to the sample surface, z = 200 nm). d): w = 485 nm, e) w = 175 nm, and f) w = 80 nm. Reproduced with permission.[72] Copyright 2010, American Physical Society.

subjected in the nanostructure formed. In the simulations, the H-ion current impinging on the sample surface, the exposure duration to H, and the irradiation temperature were set equal to the experimental values. Size and shape of the heterostructures change rapidly with w, gradually approaching the nanometer size in the smallest structure. Figure 9d–f shows the spatial modulation of the bandgap energy, ΔE_g, along the growth axis z (the line scan is performed along the symmetry axis perpendicular to the wire). ΔE_g was determined using the known relationship between N concentration and the $GaAs_{1-x}N_x$ bandgap energy.[71] Importantly, for w = 80 nm, the vertical size of the wire is about 10 nm, which leads to carrier quantum confinement, as discussed next.[72]

The consequences of the reduced dimensionality are demonstrated in **Figure 10**a, which shows the PL spectra of unpatterned $GaAs_{1-x}N_x$ and $GaAs_{1-x}N_x/GaAs_{1-x}N_x$:H wire ensembles. The lattice temperature was 110 K in order to highlight the free-exciton recombination with respect to that from localized excitons, while maintaining a high narrow PL signal.[26] Upon going from the bulk to the 485 nm wire, the $GaAs_{1-x}N_x$ PL signal was roughly constant, while in the case of the 175 nm structures the integrated intensity of the $GaAs_{1-x}N_x$ luminescence increases slightly by a factor of 1.6. In the case of the 80 nm wires, instead, the $GaAs_{1-x}N_x$ integrated intensity increases dramatically by a factor of 50 and blue-shifts. This increase in the $GaAs_{1-x}N_x$ PL integrated intensity for constant number of photoexcited carriers has to be attributed to an enhanced radiative efficiency. This is a signature of an increased electron-hole wavefunction overlap due to sizable carrier confinement in the nanostructures. Most importantly, the PL peak of the smallest wires blueshifts by about 30 meV with respect to the untreated sample and the larger wires, which is further evidence of quantum confinement. The above-mentioned value matches well with the quantum confinement energy estimated for a 10 nm-thick $GaAs_{1-x}N_x$ (x = 0.9%) quantum well sandwiched in GaAs barriers (10 nm is the average thickness of the $GaAs_{1-x}N_x$ wire as it results from the data displayed in Figure 9f).

In order to further investigate this effect, we used time-resolved μ-PL. Figure 10b shows the time evolution of the emission at T = 10 K for different single wires (symbols) and for the unpatterned sample (solid line). The detection energy is set at the maximum of the free-exciton band, as measured by continuous-wave μ-PL (1.40 eV for w = 80 nm and 1.32 eV for w = 175 nm and 485 nm and the as-grown sample). Different laser power densities were used for different w's in order to keep the same density of photogenerated carriers, $n_{photogen}$, and thus to compare carrier dynamics consistently in the various structures. An estimate of the density of photogenerated carriers can be obtained by $n_{photogen} = \alpha (h\nu) N_{ph}/s^2$, where $\alpha \approx 10^5$ cm^{-1} is the absorption coefficient of GaAs at the exciting wavelength (600 nm) and s is the laser spot size (about 1.5 μm). Finally, one finds $n_{photogen}$=1.0 × 10^{20} cm^{-3}. This large number can, indeed, lead to band-filling effects, as observed experimentally in the narrowest wires. The behavior of the w = 485 and 175 nm wires is similar to that of the as-grown sample and the three decay curves overlap in Figure 10. For w = 80 nm the μ-PL intensity exhibits an overall longer decay with a pronounced plateau. This plateau is a fingerprint of band-filling effects, which usually take place in low-dimensional systems because of a reduced density of states.[73,74] In fact, carrier replenishment of the ground state from higher energy states is slowed

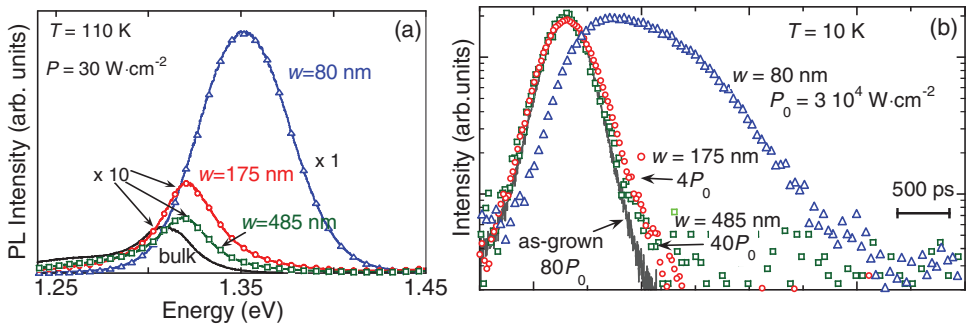

Figure 10. a) PL spectra recorded at $T = 110$ K for a same laser power density ($P_0 = 30$ W cm^{-2}) on bulk $GaAs_{1-x}N_x$ (gray line, least intense spectrum) and $GaAs_{1-x}N_x/GaAs_{1-x}N_x$:H wires with different width w equal to 485, 175, and 80 nm (line + squares, circles, and triangles, respectively). Notice the large increase in the PL signal in the narrowest wire. b) Low-temperature ($T = 10$ K), time-resolved μ-PL spectra on the same single wires as in panel (a), obtained by setting the detection energy at the free-exciton recombination energy (1.40 eV for $w = 80$ nm; 1.32 eV for $w = 175$ nm, 485 nm, and the as-grown sample). Different laser power densities have been used to maintain the same density of collected photogenerated carriers in the different wires.

by the breaking-up of the bulk continuum levels into discrete levels (along at least one dimension in our case).

4.2. From 2D to 0D

4.2.1. Quantum Dot Fabrication and Optical Characterization

A further reduction of the dimensionality of the carrier potential can be achieved using masks that allow control of hydrogen diffusion in two dimensions.[49] This is shown by the 3D simulation in **Figure 11**a, where a $GaAs_{1-x}N_x$ quantum well ($x = 1.1\%$, $t = 6$ nm, distance from surface equal to 30 nm) is covered by an ensemble of Ti dots with diameter $d = 80$ nm. After exposure (duration equal to 420 s) to a H-ion current density equal to 30 μA cm^{-2} at temperature $T_H = 200$ °C, a H-free region about 50 nm in diameter and 3 nm high is formed in the area beneath each dot. According to Figure 11a this nanometer-sized

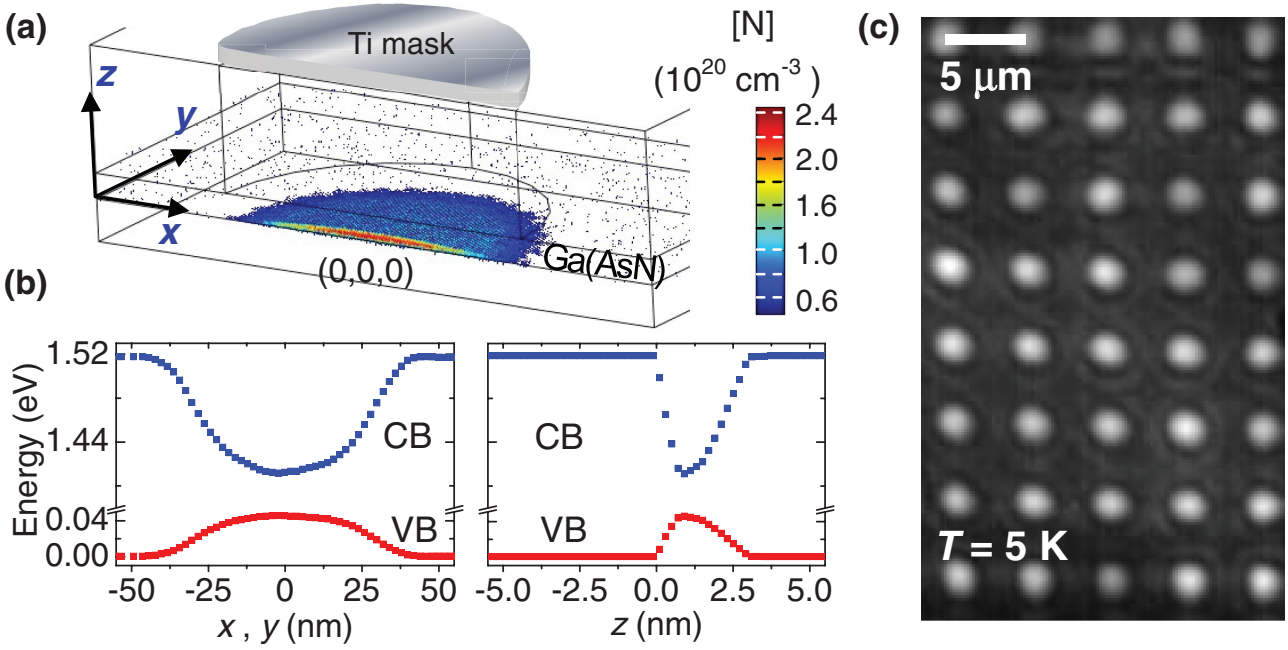

Figure 11. a) 3D distribution of N atoms not passivated by H (namely, N atoms without bound H atoms) obtained after a masked hydrogenation of a $GaAs_{1-x}N_x$ quantum well with thickness $t = 6$ nm and $x = 1.1\%$. The axis origin (0,0,0) is set in the dot center at the $GaAs_{1-x}N_x/GaAs$ buffer interface. b) Energy band diagrams in the conduction (CB) and valence band (VB) as obtained by performing a linescan along the dot symmetry axes (the scan along the x- or y-axis was done at a dot height $z = 1$ nm). The diagrams were derived from the relationship between the effective N concentration (namely, the density of N atoms with no bound H atoms) and the $GaAs_{1-x}N_x$ bandgap energy. The conduction band offset was taken to be equal to 0.7. Due to the requested large calculus power, only half a dot is displayed and large meshes are employed, thus causing a lower spatial accuracy with respect to the two-dimensional case. c) $T = 5$ K PL image of an ensemble of $GaAs_{1-x}N_x$ dots obtained using the technique depicted in the Figure 7 and 9 and using Ti dots with $d = 80$ nm. The image was recorded using an 850 nm low-energy pass filter to reject the emission from the GaAs cap and buffer layer and from the hydrogenated $GaAs_{1-x}N_x$ barriers. The single-dot image size is determined by the carrier diffusion length. The PL image demonstrates excellent control over the dot position and a quite uniform emission efficiency from the array. Reproduced with permission.[49]

region has the composition of the starting $GaAs_{1-x}N_x$ material (bandgap energy E_g = 1.32 eV at 5 K) and is surrounded on all sides by a GaAs or hydrogenated-$GaAs_{1-x}N_x$ barrier (E_g = 1.52 eV at 5 K). We point out that the chosen dimensions of the metallic pattern do not require a cutting-edge lithographic apparatus since it is H diffusion that determines the actual dot size, which is ultimately smaller than the diameter d of the Ti dot deposited on the sample surface. The known relationship between the N concentration and the bandgap energy[71] leads to the conduction and valence band diagrams shown in Figure 11b. Panel (c) shows a μ-PL image at low-temperature (5 K) of an array of $GaAs_{1-x}N_x$ dots obtained by the technique just described using metallic dots with d = 80 nm. The image demonstrates excellent control over the dot position and exhibits a very uniform emission efficiency.

To address the electronic properties of a single nanostructure, we performed μ-PL measurements. It is worth remarking that the very small density of nanostructures achievable by our method (for instance 4×10^6 dots cm^{-2}, see Figure 11) permits investigation of a single emitter without the need for chemical isolation of the nanostructure, metallic masks with apertures, or the use of optical setups with high spatial resolution. Furthermore, the dots so-fabricated have no surfaces exposed to air, which are detrimental for the emission yield in self-assembled nanocrystals and lithographic nanostructures.[75,76] In fact, H causes negligible damage at the H doses used here and, on the contrary, it often leads to an improvement in the PL efficiency.[27] **Figure 12**a shows the μ-PL spectra at 5 K of a single nanostructure formed starting from a Ti dot with d = 80 nm and of the starting quantum well sample. Laser power densities equal to 5.0 W cm^{-2} and 0.75 W cm^{-2} were used for the dot and bulk samples, respectively. Dramatic changes can be noticed: the dot emission is blue-shifted by about 70 meV with respect to the untreated material and the PL linewidth of the dot is more than two orders of magnitude smaller than that of the starting sample. This is in agreement with an estimate obtained by treating the dot potential as a decoupled square box with finite height barriers and using the dot geometrical parameters displayed in Figure 11a.

Panels (b,c) show the effect of different perturbations addressing the 0D nature of the recombining carriers. In panel (b) the dependence of a single dot PL spectrum on the density of photogenerated carriers is shown. At the lowest laser power, P, a single line at 1.402 eV due to the ground state exciton dominates the spectrum. With increasing P, the intensity of low-energy (<1.402 eV) components increases more rapidly than that of the ground state exciton. These additional lines can be attributed to biexciton and charged/multiple exciton recombination, as in other QD-like systems.[77–79] At higher laser power, the intensity of single- and bi- (multiple)-exciton recombination lines becomes progressively saturated and other distinct states appear at higher energy. This behavior, widely reported in many 0D systems, is typical of a population of excited states.[77]

Figure 12c shows the μ-PL spectra at 5 K of a d = 80 nm dot (similar to that shown in the previous panel) and of the corresponding untreated sample as a function of magnetic field in the B = 0–30 T interval (the laser power density was 30 W cm^{-2}). The magnetic field is applied along the growth axis. The extent and functional dependence of the variation of the recombining carrier energy with magnetic field provides information on the dimensionality and symmetry of the confining potential to which carriers are subjected in a nanostructure.[80] In the untreated sample, a B-induced shift of about 15 meV is observed. In the d = 80 nm dot, the exciton line shifts with B much less (2 meV) than in the $GaAs_{1-x}N_x$ QW. This clearly indicates that carriers in the dot undergo a strong spatial localization/confinement, resulting in a smaller wavefunction size. Furthermore, a clear spin-splitting can be observed in the dot. Panel (d) displays a quantitative analysis of the diamagnetic shift, ΔE_d, data for the QD. In a perturbative framework that holds for tightly bound electron–hole pairs as in atomic-like systems, the B-induced variation of the exciton energy is given by $\Delta E_d = \left(e^2/8\mu_{exc}\right) < \rho_{exc}^2 > B^2 = \beta B^2$,[81] where e is the electron charge, μ_{exc} is the exciton reduced mass, and ρ_{exc} is the wavefunction extent in the plane perpendicular to B. ρ_{exc} is related to the exciton diameter by $d_{exc} = \sqrt{2 < \rho_{exc}^2 >}$. If μ_{exc} (= $0.095m_0$, where m_0 is the electron mass in vacuum)[8] depends on the sample composition only, we obtain d_{exc} = 4.3 nm, which reflects the strong exciton confinement in the dot. Panel (d) displays also an analysis of the Zeeman-splitting data leading to a value of the exciton g-factor equal to 1.04.

4.2.2. Dependence of Quantum Dot Emission on Local Electric Fields and Temperature

One of the main advantages of the method discussed here is the possibility to fabricate nanostructures with size and site that can be controlled with nanometer precision. This method does not require lengthy, repeated, and complicated lithographic processes (except for the deposition of the metallic mask) that are typical in top-down approaches[82] and, at the same time, circumvents the random character of the nanostructure formation typical of bottom-up growth techniques.[83] However, $GaAs_{1-x}N_x$ dots exhibit a relatively large (0.2 meV) linewidth that may be detrimental for photonic applications, where spectral purity is an important issue. This is in part due to local electric fields that perturb the carrier confining potential and gives rise to spectral diffusion effects. **Figure 13** shows the temporal evolution of a single dot μ-PL spectrum. The peak energy wanders by more than 1 meV and PL intensity changes. This effect has been reported in other quantum dot systems, such as II-VI nanocrystals, and is attributed to a charged QD environment that changes with time under optical pumping.[84] In our case, the local electric fields are likely due to the presence of hydrogen atoms in the QD surrounding. We know that a third H atom, whose spatial position is unknown yet, induces a compressive strain (see Section 3.1). This H atom can be removed after a mild annealing that leaves the N-passivating C_{1h} complex untouched. Different hydrogenation/annealing procedures are being attempted in order to minimize these spectral diffusion effects and to considerably reduce the single dot emission linewidth. Alternatively, resonant excitation below the GaAs barrier could lead to a lowered broadening of the dot emission line.

Another important issue concerns the thermal stability of the quantum dot emission yield. **Figure 14**a shows the μ-PL spectra of a single dot (d = 80 nm) as a function of temperature up to T = 110 K and at a laser power density equal to 25 W cm^{-2}.

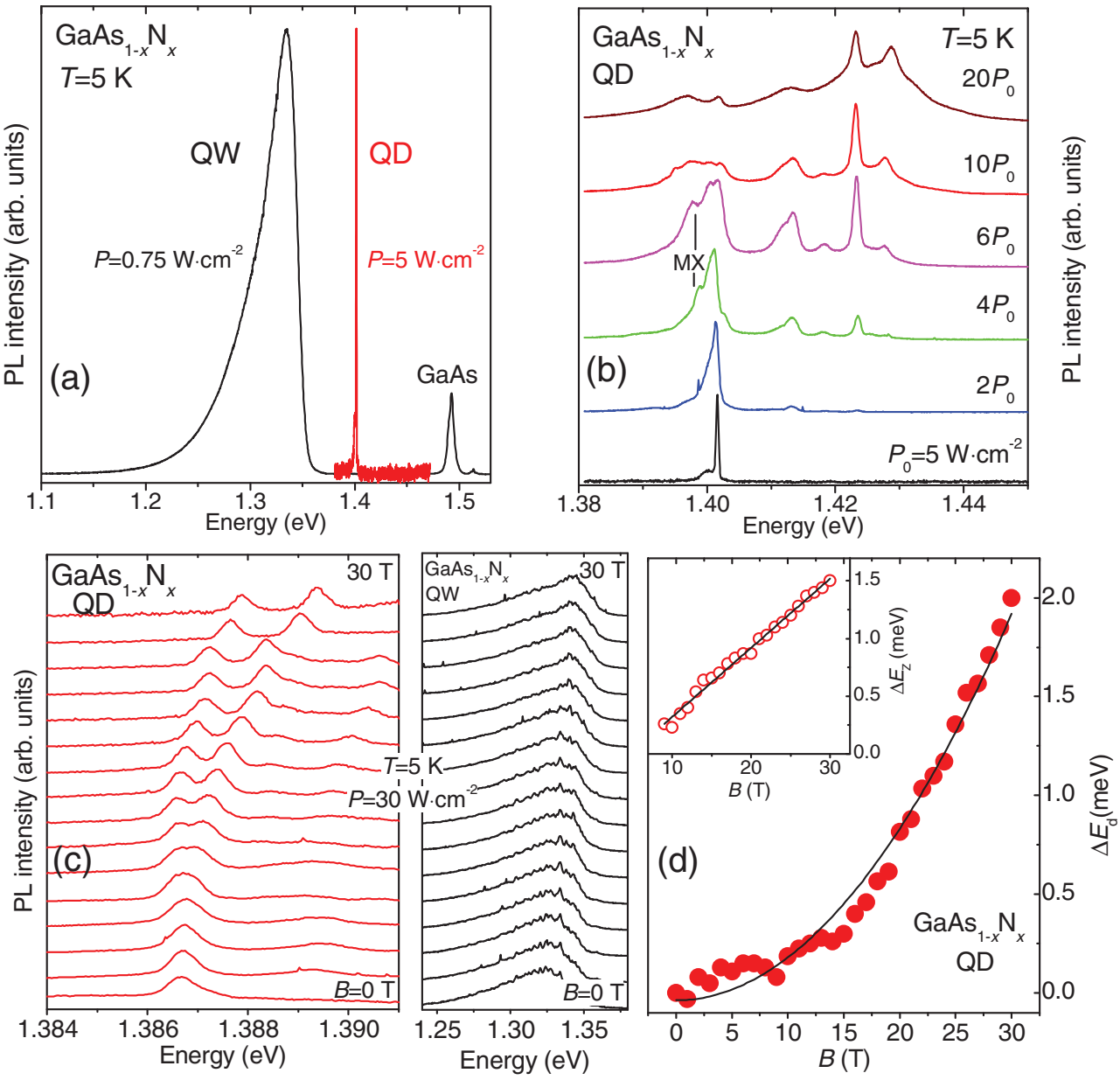

Figure 12. a) Low-temperature PL spectra of a untreated $GaAs_{1-x}N_x$ quantum well (x = 1.1%, well thickness equal to 6 nm) and of a single dot fabricated using the same quantum well as the starting material and following the fabrication method outlined in Figure 11. b) Low-temperature μ-PL spectra for different excitation powers on the same single dot shown in panel (a). MX indicates multiexcitonic components as discussed in the text. c) Low-temperature (T = 5 K) μ-PL spectra for different magnetic fields, B, recorded on a single dot similar to that shown in panels (a,b). The right panel refers to the starting quantum well material displayed in panel (a), while the left panel refers to a single dot. Note the large energy scale difference. The spectra are displayed in steps of 2 T. d) Diamagnetic shift, ΔE_d , of one dot (circles indicate the average of the Zeeman split components). Lines are fits to the data according to the diamagnetic shift formula $\Delta E_d = \beta B^2$ reported in the text. The error associated to each data point is within the symbol size. The inset shows Zeeman splitting, ΔE_Z , data for the dot. The line is a fit to the data according to $\Delta E_Z = g_{exc}\mu_B B$, where g_{exc} is the exciton g-factor and μ_B is the Bohr's magneton.

This demonstrates that, despite the relatively low confining potential, the optical quality of these QDs is remarkably good. At the lowest temperature two levels in thermal equilibrium, separated by 6 meV and ascribable to the the light- and heavy-hole excitons forming in the QDs, can be observed. It is rather difficult to estimate which of the valence bands is involved in the lowest energy transition. Indeed, the energy splitting of the two lines is a result of two counterbalancing effects. On the one hand, quantum confinement tends to push the light hole towards higher energy with respect to the heavy hole due to the different effective masses. On the other hand, the compression caused by the H-induced barrier expansion

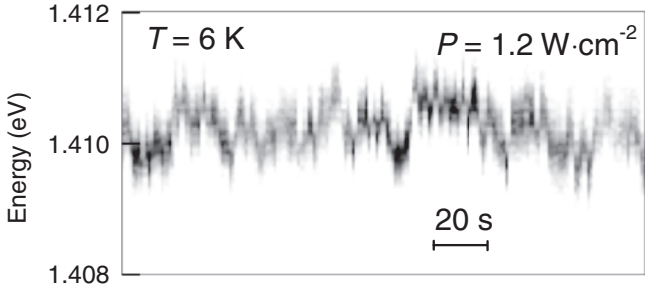

Figure 13. μ-PL spectra from a single $GaAs_{1-x}N_x$/GaAs QD with d = 80 nm recorded as a function of time at T = 6 K and at a power density of 1.2 W cm^{-2}. Note that the photon energy scale runs along the vertical axis. The time interval between the different spectra is 300 ms. Brighter (darker) regions correspond minimum (maximum) PL intensity, respectively.

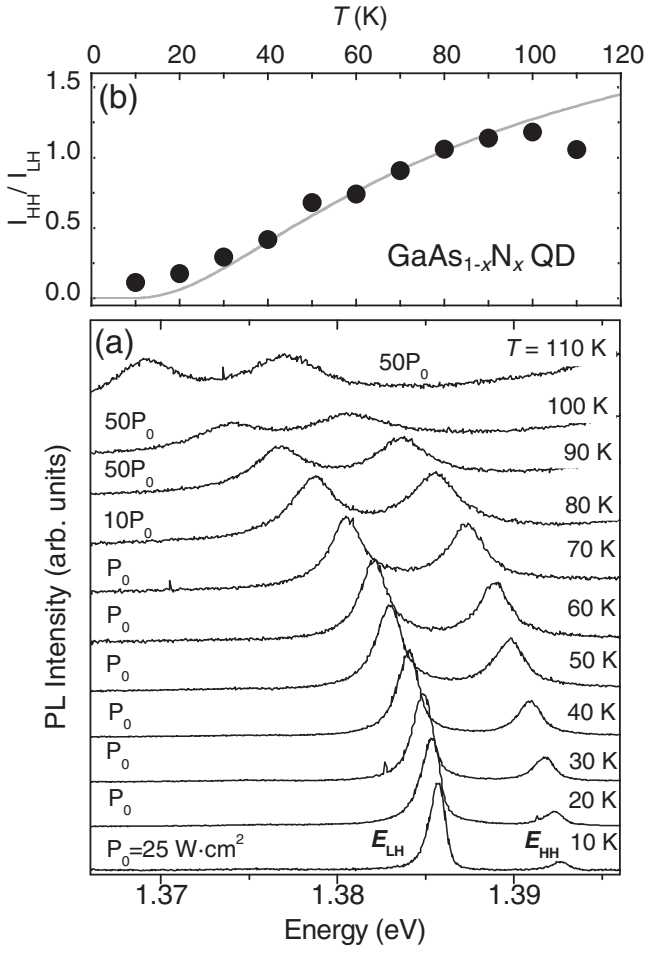

Figure 14. a) PL spectra from single $GaAs_{1-x}N_x$/$GaAs_{1-x}N_x$:H quantum dot as a function of the lattice temperature (T = 10–110 K with 10 K steps). The power density used for the measurements is also reported. Two different transitions ascribed to the light and heavy hole exciton can be clearly observed. b) Ratio between the integrated intensities of the heavy and light hole transitions (dots). The solid line indicates the theoretical curve as obtained by taking into account the different density of states of the two valence bands.

(see the next section) compensates the built-in tensile strain of the $GaAs_{1-x}N_x$ quantum well, thus reducing the "built-in" energy splitting between the valence bands. However, the evolution of the relative population of the two states as the temperature is increased suggests that the light–hole exciton is the lowest energy transition. Figure 14b shows the ratio q of the peak intensity of the two excitonic lines versus T. The line is a fit to the data by $q = 3\left(\frac{\mu_{HH}}{\mu_{LH}}\right)^{\frac{3}{2}} e^{-(E_{HH}-E_{LH})/(k_B T)}$, where the pre-factor 3 takes into account the different density of states of light- and heavy-hole excitons having reduced mass equal to μ_{LH} and μ_{HH}, respectively,[85] while $\left(\frac{\mu_{HH}}{\mu_{LH}}\right)^{\frac{3}{2}} = M$ is the ratio between the exciton reduced masses and is left as a fitting parameter. A good agreement is found with the experimental data by using the previous formula with M = 0.93. This value is very close to what we find for strained bulk material (see the next section), where the lowest energy transition has a predominant light hole character.[85]

5. Strain-Engineering in $GaAs_{1-x}N_x$/$GaAs_{1-x}N_x$:H Heterostructures

The possibility of controlling strain fields in semiconductor heterostructures is a key issue in modern solid state physics. Strain has a remarkable effect on the band structure of bulk semiconductors,[86] it plays a fundamental role in the growth and in the determination of the physical properties of Stranski–Krastanov quantum dots,[87] and it can lead to surprising polarization effects for the light emitted by semiconductor quantum wires.[88]

We have already mentioned that H irradiation results in the formation of H–N complexes, which cause an astonishing expansion of the $GaAs_{1-x}N_x$ cubic cell and induce a reversal of the strain status of the $GaAs_{1-x}N_x$ layer from tensile to compressive.[41,42,44] This finding opens up the unprecedented possibility to spatially modulate strain fields in the growth plane of $GaAs_{1-x}N_x$ heterostructures by the masking-hydrogenation procedure presented so far, thus paralleling the effect on the bandgap. This section is entirely devoted to this subject. We have found that the extent and the direction of the strain fields can be tailored by the size and shape of the patterned $GaAs_{1-x}N_x$ structures and by sample composition. The resulting in-plane structural anisotropy switches on polarization selection rules that hold for photons emitted along the growth axis. This allows for tight control of the polarization properties of the light emitted by submicrometer-sized $GaAs_{1-x}N_x$ wires. The experimental findings are quantitatively accounted for by combining finite-element stress calculations with optical selection rules.

We studied 200 nm-thick $GaAs_{1-x}N_x$ layers (x = 0.4%–0.9%) grown on (001) GaAs. A 50 nm-thick film of titanium was deposited on the $GaAs_{1-x}N_x$ surface and patterned by electron beam lithography. Samples were hydrogenated at 300 °C. The lowest H dose necessary to passivate the entire unpatterned $GaAs_{1-x}N_x$ layer was used for all the samples studied here. As described in Section 3.2, H proceeds into $GaAs_{1-x}N_x$ by a trapping-limited diffusion with a H forefront of 10 nm per decade, or less. Therefore, steep $GaAs_{1-x}N_x$/$GaAs_{1-x}N_x$:H interfaces are obtained.

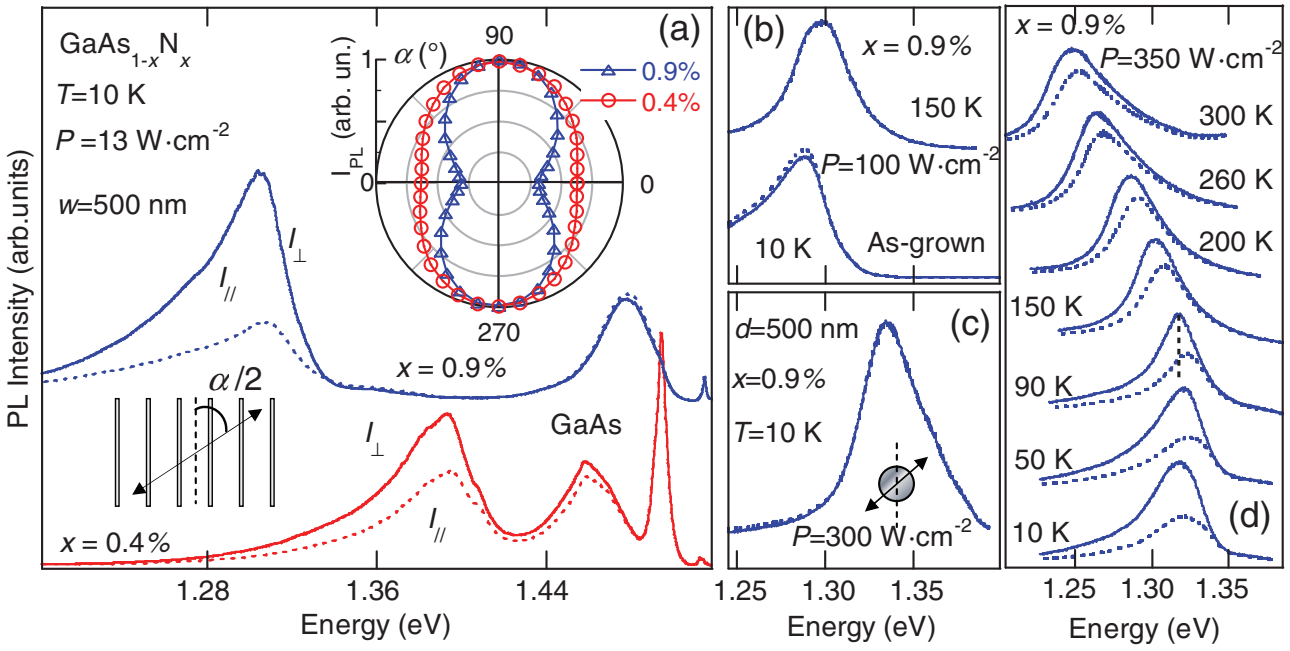

Figure 15. a) PL spectra taken at $T = 10$ K on ensembles of $GaAs_{1-x}N_x$ wires with $x = 0.9$ and 0.4% (width $w = 500$ nm for both samples) for light polarization perpendicular ($I_\perp$, solid lines) and parallel ($I_{//}$, dotted lines) to the wire axis, which is assumed to be oriented along the [110] direction. Bottom-left inset: Sketch of the metallic pattern deposited before H irradiation. Top-right inset: Polar plot of the normalized PL intensity (I_{PL}) as a function of the angle α formed between the linear polarizer and the wire axis (see inset bottom-left inset). Notice that the dependence of the optical setup on the polarization is eliminated by the combined use of a fixed polarizer plus a $\lambda/2$ wave-plate. b) PL spectra for the as-grown $GaAs_{1-x}N_x$ sample ($x = 0.9\%$) at two different temperatures ($T = 10$ K and $T = 150$ K, bottom and top spectra, respectively) and for light polarization perpendicular ($I_\perp$, solid lines) and parallel ($I_{//}$, dotted lines) to the [110] axis. No polarization anisotropy is observed in the spectra obtained at $T = 150$ K. c) PL spectra taken at $T = 10$ K on ensembles of $GaAs_{1-x}N_x$ dots with $x = 0.9\%$ and diameter equal to 500 nm for light polarization perpendicular ($I_\perp$, solid lines) and parallel ($I_{//}$, dotted lines) to the [110] axis. No polarization anisotropy is observed. The spectra of the dots are blue-shifted with respect to those of the as-grown sample. This is most likely due to the diffusion of hydrogen through the whole dot. d) PL spectra acquired at different temperatures ($T = 10$–300 K) on ensembles of $GaAs_{1-x}N_x$ wires with $x = 0.9\%$ ($w = 500$ nm) for light polarization perpendicular ($I_\perp$, solid lines) and parallel ($I_{//}$, dotted lines) to the wire axis. The vertical dashed line highlights the presence of an energy splitting between the spectra obtained by selecting different polarization.

Figure 15a shows polarized PL spectra of $GaAs_{1-x}N_x$/$GaAs_{1-x}N_x$:H wires at $T = 10$ K. The top and bottom spectra were recorded on a 800×800 μm^2 ensemble of $GaAs_{1-x}N_x$ wires with $x = 0.9\%$ and 0.4%, respectively. The wires were 500 nm wide, separated by 5 μm and directed along the [110] or [1–10] directions. The lowest energy band is due to carrier recombination in the $GaAs_{1-x}N_x$ wires, while other luminescence bands are due to carrier recombination from hydrogenated $GaAs_{1-x}N_x$ (GaAs-like) regions aside the wires. Solid and dashed lines refer to light polarized perpendicular and parallel to the wire axis, respectively. The light emitted from $GaAs_{1-x}N_x$ wires is preferentially polarized perpendicularly to the wire axis (independently of being directed along [110] or [1–10] directions). This immediately excludes the quantum confinement effect as the source of the observed anisotropy.[89] The top-right inset shows a polar plot of the normalized PL intensity as a function of the angle, α, formed between the linear polarizer and the wire axis (see inset Figure 15a). $I_{//}$ and $I_\perp$ indicate the PL peak intensity measured parallel (0° and 180°) and perpendicularly (90° and 270°) to the wire axis, respectively. This figure highlights that the light emitted by $GaAs_{1-x}N_x$ wires is mainly polarized perpendicularly to the wire axis and that the polarization degree strongly depends on the sample composition. In order to verify the genuineness of our results, several control experiments were performed. First, the polarization properties of the light emitted from the untreated sample were studied. As shown in Figure 15b, we found a small (5%) polarization degree at 10 K. This result is not surprising as it is well known that the low temperature PL spectrum of dilute $GaAs_{1-x}N_x$ is dominated by localized states, which may exhibit some polarization anisotropy.[90] This picture is further supported by the temperature dependence of this built-in anisotropy, which disappears as soon as the contribution of localized states in the PL spectrum becomes negligible (see top spectra of Figure 15b). Furthermore, an ensemble of circular dots in the $x = 0.9\%$ sample, which shows the highest polarization anisotropy, were also patterned. The single dot is separated from the others by 5 μm and has diameter equal to 500 nm. The low-temperature polarized PL spectra of the dot ensemble are shown in Figure 15c. No polarization is observed in these highly symmetric structures, thus indicating that the sample structuring is responsible for the observed polarization anisotropy and this definitively rules out any spurious effect. Notice that the spectra of the dots are blue shifted with respect to those of the as-grown sample due to H-induced passivation of localized states, which leads to the predominance of the free-exciton contribution in the PL. Further information can be extracted from temperature-dependent PL measurements on ensembles of $GaAs_{1-x}N_x$ wires

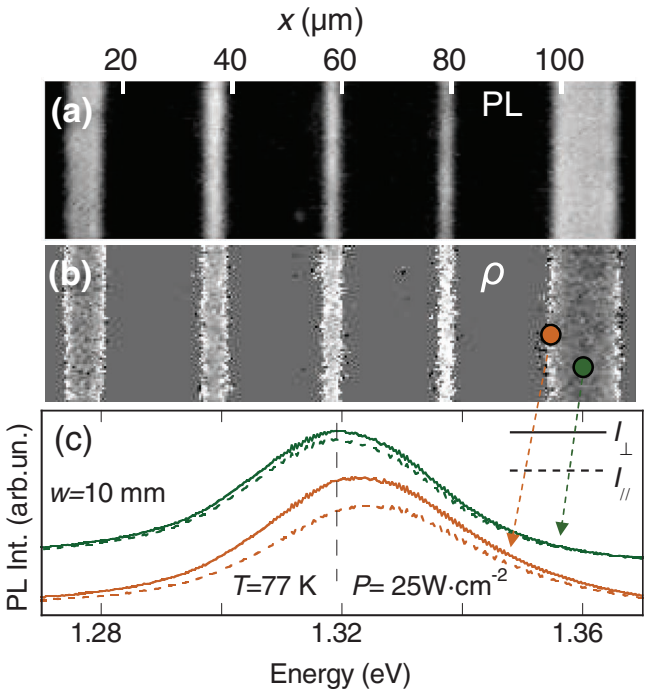

Figure 16. a) Photoluminescence, PL, imaging of 5.0, 2.0, 1.0, 0.5, and 10 μm-thick $GaAs_{1-x}N_x$ wires, from left to right; white (black) corresponds to maximum (minimum) intensity. b) Spatial map of the PL polarization degree (ρ) on the same area shown in (a); white (black) indicates maximum (minimum) ρ. Note the higher value of ρ at the wire borders. c) T = 77 K μ-PL spectra recorded at power density of 25 W cm^{-2} at the center (top spectra) and border (bottom spectra) of a 10 μm wide wire for light polarization parallel ($I_{//}$) and orthogonal ($I_{\perp}$) to the wire axis. The vertical dashed line highlights the relative shift of the PL peak positions.

(see Figure 15d). Although a progressive decrease in the polarization degree is observed, we still measure $\rho \approx 20\%$ at room temperature, thus demonstrating that the polarization effect in the wires involves both extended and localized states. Furthermore, an energetic splitting between the spectra obtained with light polarized perpendicular and parallel to the wire axis is clearly observed for $T > 50$ K, where excitonic transitions dominate PL spectra. The PL band is thus composed by transitions with different selection rules for light polarized in the crystal growth plane, which should be related to the strain-split valence band states. This indicates that strain is playing a key role in these experiments.

In order to address the physical origin of the macroscopic polarization anisotropy measured in the wire ensemble, we next focus on the local polarization properties of isolated wires. **Figure 16**a shows the μ-PL intensity imaging at liquid nitrogen temperature T = 77 K of $GaAs_{1-x}N_x$ wires with x = 0.9% and width w = 5.0, 2.0, 1.0, 0.5, and 10 μm (this temperature and the use of a highly focused laser beam ensures a scarce contribution of localized states). Brighter and darker regions correspond to maximum and minimum intensity, respectively (the luminescence from $GaAs_{1-x}N_x$:H bands was rejected by a GaAs filter placed in front of the detector). Figure 16b shows a map of the polarization degree for $\alpha = 0°$ recorded on the same sample zone. For $w > 1$ μm, these data clearly show that the polarization anisotropy observed in the ensemble is mainly located at the wire borders. For the smallest stripes, the interfaces merge in a single peak and, simultaneously, the polarization degree increases. Finally, Figure 16c shows that the spectra recorded at the edge of the w = 10 μm wire are blue-shifted (and have greater polarization degree) with respect to the spectra recorded at the centre of the same wire. This explains the energy splitting already observed in the ensemble spectra of the smallest wires and it suggests the presence of a compressive strain at the wire borders.[86] A rather clear physical picture is emerging: the strain modulation in the planar heterostructures arises from the hydrogen-induced expansion of the barriers against the $GaAs_{1-x}N_x$ wires. This introduces a marked in-plane structural anisotropy, which induces an optical anisotropy for the polarization of the light emitted in the crystal growth direction.

In order to support this picture, finite element calculations in the framework of thermoelasticity were employed to estimate the strain experienced by the wires. We model the strain distribution by considering the deformation induced on a $GaAs_{1-x}N_x$ wire by the thermal expansion of the adjacent $GaAs_{1-x}N_x$:H barriers.[52] The extent of the thermal expansion is fixed by the experimental values of the compressive (tensile) strains measured in unpatterned $GaAs_{1-x}N_x$:H ($GaAs_{1-x}N_x$) samples by high-resolution X-ray diffraction.[41,42,44] **Figure 17**a shows the 3D distribution of the strain field, ε_{xx}, calculated in a 2 μm $GaAs_{1-x}N_x$ wire with x = 0.9% and laterally delimited by hydrogenated barriers. According to our qualitative picture, the

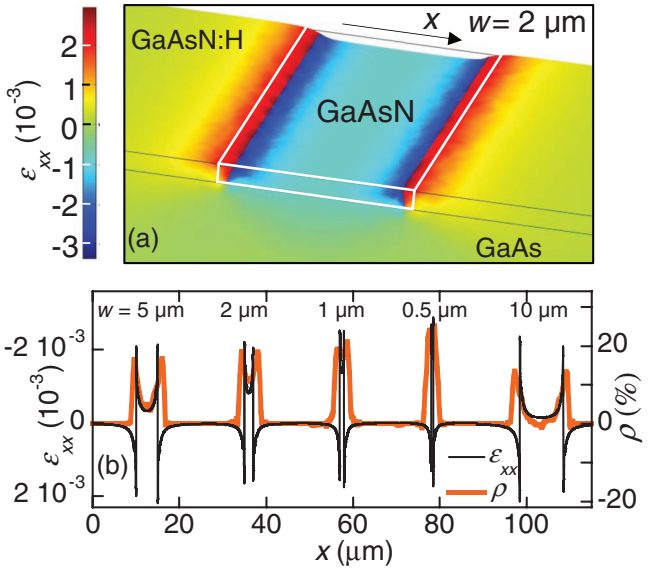

Figure 17. a) 3D distribution of the strain field, ε_{xx}, calculated along the direction perpendicular to the axis of a w = 2.0 μm $GaAs_{1-x}N_x$ (x = 0.9%) wire embedded between $GaAs_{1-x}N_x$:H barriers (structure deformation is magnified 100 times); refer to Figure 7 for the fabrication process. The picture shows a portion of the wire cut along the coordinate x. b) Line scan of calculated strain field ε_{xx} along the normal to the wire axis (thin black line, left axis; note the inverted ordinate). Note the qualitative agreement with the experimental polarization degree ρ shown in Figure 16c (thick line, right axis). Reproduced with permission.[51] Copyright 2009, American Institute of Physics.

expansion of the barriers against the wire is reproduced. The same calculations were extended to the structure described in Figure 16. Figure 17b shows a line scan of ε_{xx} along the direction perpendicular to the wires together with a line scan of the polarization degree as obtained after a vertical binning of the polarization map displayed in Figure 16b. A remarkable agreement between the polarization degree and the strain is found. This proves the close connection between the optical anisotropy and the strain modulation and calls for a quantitative analysis. Nevertheless, the simple and well-established optical selection rules for uniaxial stress applied along highly symmetric directions, such as [001] and [111], do not hold in the present case, since strain takes place along the [110] or [1–10] crystal directions. This leads to a complicated form of the orbital-strain Hamiltonian and the projection of the total angular momentum along the quantization axis, m_J, is no longer a good quantum number. This induces a mixing of the two top-most valence bands, which can be written in the [110] representation as:[91]

$$u_{v1} = c_a\,|3/2;3/2\rangle_{110} + c_b\,|3/2;-1/2\rangle_{110}$$
$$u_{v2} = -c_b\,|3/2;3/2\rangle_{110} + c_a\,|3/2;-1/2\rangle_{110}\,. \quad (7)$$

c_a and c_b depend on the elastic constants, the uniaxial deformation potentials, and, most importantly, the ratio $\sigma_\perp/\sigma_{//}$ between the stress components perpendicular and parallel to the wire axis. ρ can be calculated from the transition matrix element between the conduction band states u_c and the valence band states u_{v1} and u_{v2}. These matrix elements depend on the orientation of the polarization vector of the emitted light, $\hat{\varepsilon}^{//,\perp}$, with respect to the wire axis:[85]

$$M_i^{//,\perp} \propto \left|< u_c|\,\hat{\varepsilon}^{//,\perp}\cdot\vec{p}\,|u_{vi}>\right|^2 \;(i=1,2) \quad (8)$$

Then, each transition is weighted by the corresponding reduced density of states (proportional to $\mu_i^{3/2}$, where μ_i is the exciton reduced mass) and by the relative thermal population of the valence band states $e^{-\delta E_{12}/(k_B T)}$, where δE_{12} is the calculated energy separation between u_{v1} and u_{v2}.[92] Finally one finds:

$$I_{//,\perp} \propto [\mu_1^{3/2} M_1^{//,\perp} + \mu_2^{3/2} M_2^{//,\perp} e^{-\delta E_{12}/(k_B T)}] \quad (9)$$

According to Equations (7–9), the polarization degree, which can be calculated from Equation (9), depends via Equations (7,8) on $\sigma_\perp/\sigma_{//}$. This latter quantity can be used to explain all the experimental results presented so far, since it accounts for the sample structuring. In unpatterned, tensile strained $GaAs_{1-x}N_x$ samples and in highly symmetric structures (such as the dots presented in Figure 15) $\sigma_\perp = \sigma_{//}$. In this case, the in-plane symmetry is not broken and there is no optical anisotropy for photons whose polarization vector lies in the (001) plane. In $GaAs_{1-x}N_x$ wires, the compression caused by the expansion of hydrogenated barriers compensates sizeably the built-in tensile stress along one of the <110> directions (see **Figure 18**a). This breaks the symmetry in the (001) plane ($\sigma_\perp \neq \sigma_{//}$), mixes the light- and heavy-holes states (see Equation (7)) and switches on optical selection rules for light emitted along the crystal growth direction (see Equation (8)). $\sigma_{//}$ and $\sigma_\perp$ determined at the center of the wire by finite element calculations are shown versus w in Figure 18b). As expected, $\sigma_\perp$ changes with w while $\sigma_{//}$ remains essentialy constant. Finally, Figure 18c shows the

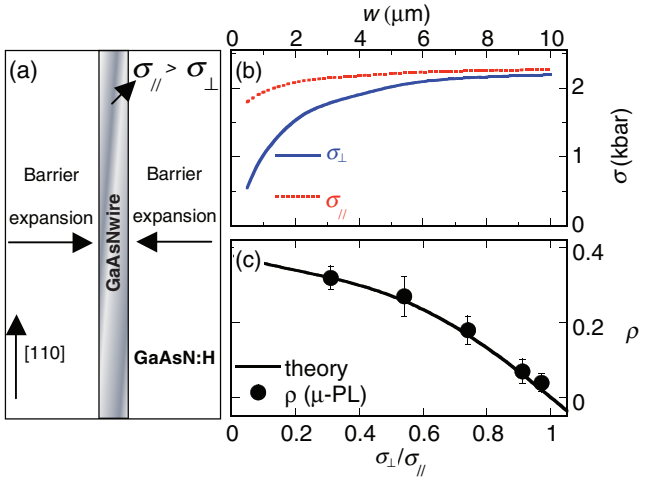

Figure 18. a) Sketch of a $GaAs_{1-x}N_x$ wire embedded between $GaAs_{1-x}N_x$:H barriers. The barrier expansion against the wire induces a reduction of the built-in tensile stress along the direction perpendicular to the wire axis. The wire is assumed to be oriented along the [110] crystal direction. b) Wire width, w, dependence of the calculated stress, σ, perpendicular (solid line, $\sigma_\perp$) and parallel (dotted line, $\sigma_{//}$) to the axis of a $GaAs_{1-x}N_x$ wire (x = 0.9%) embedded between $GaAs_{1-x}N_x$:H barriers. σ was calculated at the wire center. c) Dependence on the ratio $\sigma_\perp/\sigma_{//}$ of the polarization degree ρ measured at the wire center at 77 K (symbols). The solid line is the theoretical estimation obtained by combining finite-element simulations and suitable optical selection rules.

dependence of ρ on $\sigma_\perp/\sigma_{//}$ for x = 0.9%. A very good agreement is found between the model (being μ_2/μ_1 = 1.2 the only adjustable parameter) and the polarization degree measured at the wire centre at 77 K. The value of μ_2/μ_1 found from the fit nicely parallels the one found in the previous section and suggests that the two top-most valence bands are mixed and cannot be named light and heavy holes. The same model also reproduces well the temperature dependence of ρ measured in wire ensembles (not shown here). This agreement indicates that the presented effects can be tightly controlled with promising perspectives for strain-engineered heterostructures based on $In_yGa_{1-y}As_{1-x}N_x$/GaAs and $GaP_{1-x}N_x$/GaP.

To conclude this section, we showed that the polarization properties of the light emitted by $GaAs_{1-x}N_x$ microstructures can be controlled by modulating the lattice expansion of hydrogenated $GaAs_{1-x}N_x$. This result mirrors the bandgap modulation and demonstrates that the structural properties of this class of alloys can be modelled on demand on a sub-micrometer scale.

6. Other Examples of H-Induced Variations of the Physical Properties of $GaAs_{1-x}N_x$

6.1. Refractive Index

In a semiclassical framework the refractive index of a medium in its transparency region decreases as the frequency decreases with respect to that of the so-called Sellmeier oscillator

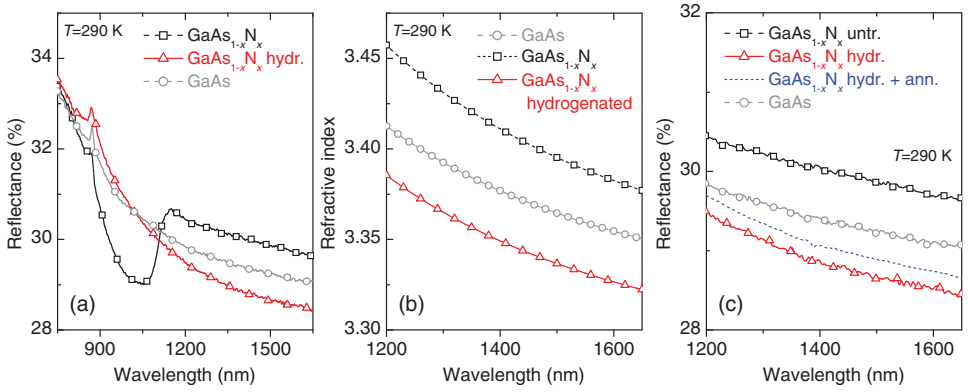

Figure 19. a) Comparison of the room-temperature reflectance spectra of a $GaAs_{1-x}N_x$ sample ($x = 2.2\%$, thickness 100 nm) before and after H-treatment and of a GaAs reference. Note the decreasing after hydrogenation of the reflectance values in the sub-gap spectral region. b) $GaAs_{1-x}N_x$ refractive index spectra before and after H irradiation, as obtained from the best fit to the reflectance spectra in the subgap region for the same sample shown in part (a). c) Reflectance spectra for a $GaAs_{1-x}N_x$ sample with $x = 0.022$ subjected to different treatments. Note the slight increase of the reflectance in the sub-gap spectral region after annealing at 225 °C, approaching the values of GaAs (N-free sample).

resonance. This resonance includes in a single classical oscillator the contribution to absorption processes occurring through the fundamental bandgap. As a consequence, one expects that the bandgap energy variation induced by hydrogen in $GaAs_{1-x}N_x$ should modify the refractive index.

Figure 19a shows a comparison of the reflectance spectra recorded at $T = 290$ K before and after H-treatment for a $GaAs_{1-x}N_x$ sample with a thickness equal to 100 nm and $x = 2.2\%$. The data of a reference GaAs are shown, too.

It is evident that the H-treated sample recovers the reflectance response typical of the GaAs-like fundamental gap, centered at 0.88 μm (≈1.4 eV). Moreover, at the same time, H irradiation decreases the reflectance of the sample in the subgap spectral region. Since the GaAs optical properties are not affected by H irradiation, this effect ought to be attributed to a decrease of the refractive index $n(\lambda)$ in the H-treated $GaAs_{1-x}N_x$ layers.

In order to obtain $n(\lambda)$ for the as-grown and hydrogenated $GaAs_{1-x}N_x$ layers in the subgap region, a best-fit procedure to the reflectance spectra was performed by using the software package WVASE32 by J.A. Woollam Co., Inc. based on the Levenberg–Marquardt algorithm. The multilayer structure of the samples was modeled with a five-phase scheme: air/2 nm oxide overlayer/20 nm GaAs cap/100 nm $GaAs_{1-x}N_x$/infinite GaAs buffer and substrate.[93] With regard to the oxide overlayer, we assumed the dielectric function of the Ga_2O_3 native oxide[94] and estimated its effective thickness by fitting the higher energy region (4–5 eV) of the spectroscopic ellipsometry curves measured on the samples. The dielectric function used for the GaAs cap, buffer, and substrate layers was taken from literature.[95] We verified that this precisely reproduces our measurements on the reference N-free GaAs epilayer.[65] The dielectric function of the GaAs cap/buffer layers was assumed not to change upon hydrogenation. This assumption relies on SIMS, which demonstrates that H incorporation is an efficient process in the N-doped layer while it is negligible outside the dilute nitride film.

Figure 19b shows the wavelength dependence of the refractive index as derived by a standard analysis of the reflectance spectra. This analysis is based on the $n(\lambda)$ dispersion in the subgap transparency region modelled through the Sellmeier relation $n^2 = A + B\lambda^2/(\lambda^2 - C) + D\lambda^2/(\lambda^2 - E)$,[96] where A was fixed while B, C, D and E were the free-variable parameters of the best fit to the reflectance spectra and λ is the wavelength (in μm). The effect of H irradiation on the $GaAs_{1-x}N_x$ refractive index is shown for a $x = 2.2\%$ sample and compared to the N-free GaAs refractive index data. For $x = 2.2\%$ the overall relative reduction of the refractive index is increased to (1.5%–2%) in the wavelength range from $\lambda = 1.3$ to 1.55 μm. These values of the refractive-index change fulfill those required for waveguiding in planar integrated optical devices.[97] Similar to what was shown for the bandgap, this effect can be engineered for in-plane optical confinement using the N concentration and post-growth H-irradiation as external tunable parameters. Very interestingly, we note in Figure 19b that upon H-irradiation the values of the refractive index of $GaAs_{1-x}N_x$ for wavelengths $\lambda > 1$ μm are significantly lower than those of the host matrix (n overshooting). The reason of the refractive index reduction (and its intriguing overshooting) in H-treated $GaAs_{1-x}N_x$ can be related to the presence of the third H atom positioned nearby the N-passivating C_{1h} complex mentioned before (see Section 2.1). Indeed, after 5 h of annealing at 225 °C we observed an increase of the reflectance of the hydrogenated $GaAs_{1-x}N_x$/GaAs structures and the R values in the subgap region become very close to those characterizing the nitrogen-free sample. Figure 19c shows the reflectance spectra of the hydrogenated $x = 0.022$ sample after annealing at 225 °C and of the sample with $x = 0.0\%$, i.e., GaAs material without compressive strain. Due to the observed tendency of the n overshoot to vanish with the reduction of the concentration of the more weakly bound hydrogen atoms, we conclude that the latter are responsible for this phenomenon.[41–42,98]

6.2. Electrical Resistance

So far, we have shown that hydrogen incorporation in $GaAs_{1-x}N_x$ determines dramatic changes of the electronic, structural, and optical properties of the material. This has led to the

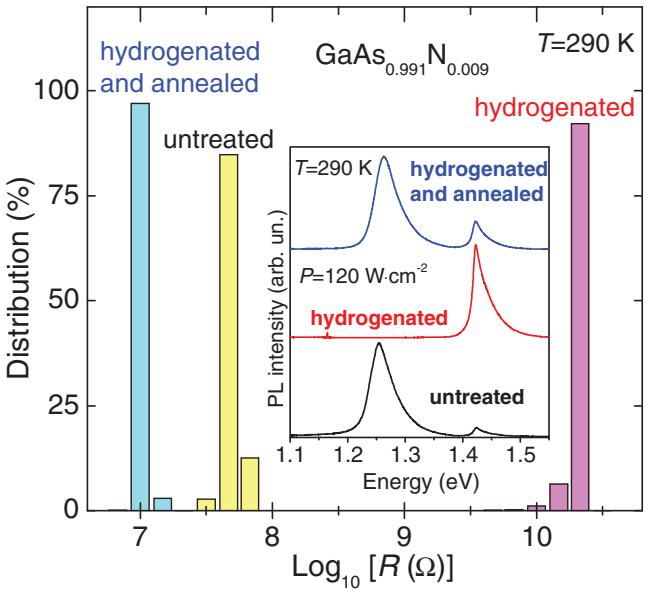

Figure 20. Histogram of local resistance R measurements on a $GaAs_{1-x}N_x$ sample (thickness 200 nm, $x = 0.9\%$ and no GaAs cap layer) subjected to different treatments, as indicated. The inset shows the room temperature PL spectra of the same samples shown in the main part of the figure. The peak at 1.255 eV is due to carrier recombination from the bandgap of untreated $GaAs_{1-x}N_x$ and of hydrogenatated $GaAs_{1-x}N_x$ after 550 °C 1 h annealing. The peak at 1.422 eV is due to carrier recombination from GaAs or fully N-passivated $GaAs_{1-x}N_x$.

fabrication of quantum dots and strained planar heterostructures and to the possibility to waveguide light by exploiting the modulation of the optical refractive index. Next, we show that also the electric and transport characteristics of these materials can be suitably modified. To this end, we used conductive-probe atomic force microscopy (CP-AFM) to measure the local resistance at room temperature.[99–101] **Figure 20** shows the local resistance, R, values measured after different treatments for a sample having $GaAs_{1-x}N_x$ thickness equal to 200 nm and $x = 0.9\%$. Hydrogen irradiation with a dose equal to 3×10^{18} cm^{-2} determines an increase of R by a factor ≈500 with respect to the untreated sample. At the same time, PL measurements at room temperature indicate a complete passivation of the electronic activity of N resulting in a blue/shift of the $GaAs_{1-x}N_x$ bandgap energy (1.255 eV) to the GaAs value (1.422 eV) (see inset in the figure). We verified that the only thermal treatment used during H irradiation (3 h at 300 °C) does not cause variation of R in the untreated material. Thermal annealing of the hydrogenated sample at 550 °C (duration 1 h) dissociates N–H complexes thus restoring the bandgap energy of the untreated $GaAs_{1-x}N_x$ sample, as shown in the inset of Figure 20. The local electrical resistance is also strongly affected by annealing treatments. In fact, R is reduced by a factor of 2000 in the hydrogenated sample after thermal treatment. This is primarily due to a removal of H atoms from the lattice. Nevertheless, we notice that the annealed sample exhibits a local resistance value smaller by about a factor 4 than that measured in the untreated (starting) material. This may be attributed to an improvement of the crystal quality caused by the high-temperature treatment. In fact, a similar R decrease has been also observed in a untreated (namely, H-free) $GaAs_{1-x}N_x$ sample subjected to a same 1 h annealing at 550 °C. We checked that the increase of the local resistance was absent in a reference N-free GaAs sample, where R was found to decrease slightly after H irradiation with an ion dose equal to that considered in Figure 20.

These results indicate that the electrical resistance of $GaAs_{1-x}N_x$ can be modulated by hydrogen irradiation in a fully controllable and reversible manner. This finding nicely parallels the effects H has on the optical and structural properties of this alloy and assigns to the N–2H complexes a rather unexpected role, that is the capability to modify even the transport properties of dilute nitrides.

An interesting outcome of our findings is the possibility to pattern the electrical properties of $GaAs_{1-x}N_x$ in its growth plane. **Figure 21**a shows an electrical resistance mapping of a series of $GaAs_{1-x}N_x$ wires with different widths, w, and formed by spatially selective hydrogenation of the $t = 200$ nm and $x = 0.9\%$ sample. R is much lower in the Ti-shielded regions than between the wires, where $R \approx 6 \times 10^{10}$ Ω (no Ti residuals were present after removal of the metallic wires, as indicated by topographic AFM images of the sample surface acquired concomitantly with the local resistance mapping). This is evident from the linear scan of R perpendicular to the wire axis and superimposed to the CP-AFM image in Figure 21a. The ratio of the resistance between the N-passivated barriers and the $GaAs_{1-x}N_x$ wires varies from a factor 750 to 15 upon changing w from 5 μm to 0.5 μm. This dependence on w is due to H diffusion beneath the metallic wires, which tends to increase the effective resistance of the considered wire. Indeed, SIMS

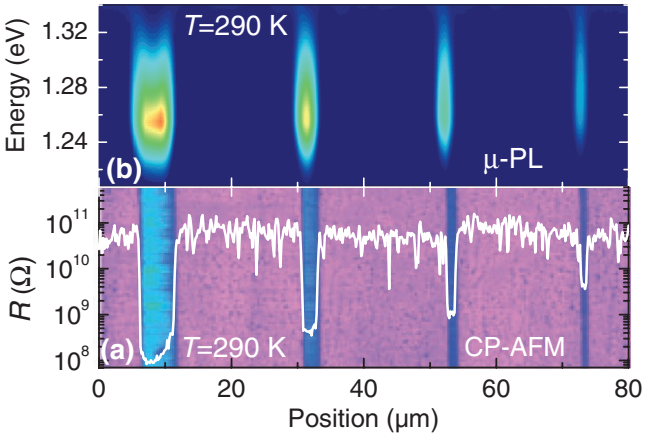

Figure 21. a) 2D mapping of the local resistance R of a $GaAs_{1-x}N_x$ sample ($x = 0.9\%$ and $t = 200$ nm) by CP-AFM. The surface was patterned before H irradiation by H-opaque titanium wires with widths equal to 5, 2, 1, and 0.5 μm (from left to right), each separated by 20 μm. The white line superimposed on the 2D map of R provides the value of the local electrical resistance (ordinate axis) along a line perpendicular to the axis of the wires. b) 1D mapping of the μ-PL intensity across the wire region recorded at room temperature (power density equal 2.5×10^4 W m^{-2}). The abscissa axis indicates the laser spot position. The ordinate axis indicates the energy of the emitted photons. The emission intensity is shown in a false color scale (red and blue correspond to maximum and minimum intensity, respectively). Reproduced with permission.[66] Copyright 2011, American Physical Society.

performed on the same sample shows a deuterium decay length equal to 12 nm per decade for a hydrogenation temperature equal to 300 °C. Combined with current spreading from the probe nanocontact, this leads to an effective resistance profile that reduces by a factor 10 within 150 nm at most at the border between hydrogenated and not-hydrogenated regions. This in-plane electrical modulation matches the spatial variation of the bandgap energy as determined by μ-PL measurements shown in Figure 21b for the same artificial structure displayed in panel (a). The wire region emits at the bandgap energy of the as-grown sample, 1.26 eV, whereas the regions aside the wire emit at higher energy (1.42 eV, not shown). The lower resistance regions of the planar heterostructure clearly coincide with those having a smaller bandgap energy. The resistance increase after hydrogenation is caused by the decrease in the intrinsic carrier density following the bandgap increase and by a decrease of the electron scattering time, as described in detail elsewhere.[66] These effects can be exploited for the realization of microscopic circuits, such as on-chip microscale coils, and electrical interconnects of more complicated nanostructures fabricated by the masked-hydrogenation procedure outlined in this work.

7. Concluding Remarks and Outlook

We have reviewed the effects of hydrogen incorporation in $GaAs_{1-x}N_x$. The capability of hydrogen to transform the whole physical properties of one material ($GaAs_{1-x}N_x$) into another (GaAs) represents a unique case in semiconductor physics. Indeed, the formation of (N–2H)–H complexes into the $GaAs_{1-x}N_x$ lattice modifies the whole band structure (bandgap energy, conduction band curvature, spin properties), the refractive index, the unit cell volume, and the electrical resistance in a fully controllable and reversible manner. Starting from the observation that H kinetics in $GaAs_{1-x}N_x$ is characterized by a highly trapping-limited motion, we implemented H-related effects in order to modulate the physical properties of the material in its growth plane. To this end, we used a masked-hydrogenation procedure, whereby the formation of N-passivating complexes can be spatially controlled. The extent to which this control can be obtained is on the order of few nanometers, as determined by mass spectrometry. Then, modelling the H diffusion permits one to fabricate site-controlled nanostructures, whose electronic properties have been investigated by PL in single nanostructures, also under high magnetic fields. A similar approach combining finite-element calculations and masked-hydrogenation has been used to engineer strain fields in $GaAs_{1-x}N_x$. This has led to a control of the polarization of the light emitted from the sample in a back-scattering geometry. We have also fabricated planar conductive, resistive, and conductive heterostructures with sub-micrometer spatial resolution, exploiting the giant increase of the electrical resistance induced by hydrogen. In a similar way, the refractive index mismatch between hydrogenated and untreated regions of a $GaAs_{1-x}N_x$ chip could be exploited to realize integrated optical waveguides.

In future work, we plan to develop the method for the fabrication of more complicated nanostructures, such as quantum rings and coupled quantum dots. In particular, the opportunity to exactly position a quantum dot in the sample growth plane opens up a series of possibilities in nanophotonics applications. For instance, a perfect matching of the position, emission energy, and polarization state of single $GaAs_{1-x}N_x$ nanostructures with the optical modes of a photonic crystal cavity would allow the achievement of efficient coupling and interesting possibilities for the realization of microcavity lasers. Furthermore, one could envision more complicated optical and electrical interconnects on a same chip using, respectively, the optical refractive index and resistance modulation, which can be obtained by patterning of hydrogen incorporation on a micrometer scale.

Finally, it is worth mentioning that the simplicity featured by our approach is of interest in other materials, for instance in graphene, whose bandgap can be tuned by hydrogen in a manner closely resembling that discovered by us in dilute nitrides,[102] or in (GaMn)As, where ferromagnetism can be spatially patterned by hydrogen, although on a micrometer scale.[103]

Acknowledgements

The authors would like to acknowledge M. Felici, F. Masia, and G. Pettinari who gave a great contribution at different stages of this research. They are grateful to A. Miriametro for his skilful and continuous technical support. The authors thank F. Martelli (IMM-CNR, Italy) and S. Rubini (TASC-CNR, Italy) for growing most of the samples presented in this work. The authors acknowledge M. Francardi, A. Gerardino, and L. Mariucci (CNR-IFN) for sample processing by electron beam lithography. Structural characterization of the samples by various experimental techniques was made possible thanks to the most fruitful collaborations with M. Berti and G. Bisognin (at Università di Padova, Italy), F. Boscherini (at Università di Bologna, Italy), G. Ciatto (at Soleil Synchrotron, Paris, France), L. Felisari (TASC-CNR, Italy), and D. Giubertoni (at Fondazione Kessler, Trento Italy). The authors acknowledge the precious collaboration with M. Stavola (at Lehigh University, USA) for insightful far infrared absorption measurements. Time-resolved measurements were performed at LENS, Firenze, Italy in collaboration with L. Cavigli, M. Gurioli, and A. Vinattieri. The refractive index measurements were performed by M. Geddo, M. Patrini, M. Galli, and G. Guizzetti (at Università di Pavia, Italy). The authors acknowledge J. Alvarez and J.-P. Kleider (at LGEP-CNRS, Paris, France) for electrical studies by conductive-probe atomic force microscopy. Finally, the authors thank A. Amore Bonapasta (IMM-CNR, Italy), P. J. Klar (at Justus-Liebig-Universität, Giessen, Germany), and E. P. O'Reilly (at NMRC, National University of Ireland, Cork) for productive collaboration and discussions. High-magnetic-field measurements were performed at the High Field Magnet Laboratory (Nijmegen, The Netherlands) and supported by EuroMagNET under the EU contract n. 228043. The authors appreciate local support in Nijmegen by J. C. Maan and P. C. M. Christianen. This work was supported by COST Action MP0805.

Received: August 21, 2011
Revised: November 18, 2011
Published online: March 16, 2012

[1] *Physics and Applications of Dilute Nitrides* (Eds: I. A. Buyanova, W. M. Chen), Taylor & Francis, New York **2004**.
[2] *Dilute Nitride Semiconductors* (Ed: M. Henini), Elsevier, Amsterdam, The Netherlands **2005.**
[3] *Dilute III-V Nitride Semiconductors and Material Systems* (Ed: A. Erol), Springer, Berlin, Germany **2008**.

[4] a) P. R. C. Kent, A. Zunger, *Phys. Rev. Lett.* **2001**, *86*, 2613; b) *Phys. Rev. B* **2001**, *64*, 115208.
[5] J. Endicott, A. Patanè, J. Ibáñez, L. Eaves, M. Bissiri, M. Hopkinson, R. Airey, G. Hill, *Phys. Rev. Lett.* **2003**, *91*, 126802.
[6] E. P. O'Reilly, A. Lindsay, P. J. Klar, A. Polimeni, M. Capizzi, *Semicond. Sci. Technol.* **2009**, *24*, 033001.
[7] U. Tisch, E. Finkman, J. Salzman, *Appl. Phys. Lett.* **2002**, *81*, 463.
[8] F. Masia, G. Pettinari, A. Polimeni, M. Felici, A. Miriametro, M. Capizzi, A. Lindsay, S. B. Healy, E. P. O'Reilly, A. Cristofoli, G. Bais, M. Piccin, S. Rubini, F. Martelli, A. Franciosi, P. J. Klar, K. Volz, W. Stolz, *Phys. Rev. B* **2006**, *73*, 073201.
[9] G. Allison, S. Spasov, A. Patanè, L. Eaves, N. V. Kozlova, J. Freudenberger, M. Hopkinson, G. Hill, *Phys. Rev. B* **2008**, *77*, 125210.
[10] T. Dannecker, Y. Jin, H. Cheng, C. F. Gorman, J. Buckeridge, C. Uher, S. Fahy, C. Kurdak, R. S. Goldman, *Phys. Rev. B* **2010**, *82*, 125203.
[11] G. Baldassarri Hoeger von Hoegersthal, A. Polimeni, F. Masia, M. Bissiri, M. Capizzi, D. Gollub, M. Fischer, A. Forchel, *Phys. Rev. B* **2003**, *67*, 233304.
[12] A. Polimeni, G. Baldassarri Hoeger von Hoegersthal, F. Masia, A. Frova, M. Capizzi, S. Sanna, V. Fiorentini, P. J. Klar, W. Stolz, *Phys. Rev. B* **2004**, *69*, 041201(R).
[13] A. Lindsay, E. P. O'Reilly, *Phys. Rev. Lett.* **2004**, *93*, 196402.
[14] P. Pichanusakorn, Y. J. Kuang, C. J. Patel, C. W. Tu, P. R. Bandaru, *Appl. Phys. Lett.* **2011**, *99*, 072114.
[15] G. Pettinari, F. Masia, A. Polimeni, M. Felici, A. Frova, M. Capizzi, A. Lindsay, E. P. O'Reilly, P. J. Klar, W. Stolz, G. Bais, M. Piccin, S. Rubini, F. Martelli, A. Franciosi, *Phys. Rev. B* **2006**, *74*, 245202.
[16] A. Kunold, A. Balocchi, F. Zhao, T. Amand, N. Ben Abdallah, J. C. Harmand, X. Marie, *Phys. Rev. B* **2011**, *83*, 165202.
[17] H. M. Zhao, L. Lombez, B. L. Liu, B. Q. Sun, Q. K. Xue, D. M. Chen, X. Marie, *Appl. Phys. Lett.* **2009**, *95*, 041911.
[18] E. L. Ivchenko, V. K. Kalevich, A. Yu. Shiryaev, M. M. Afanasiev, Y. Masumoto, *J. Phys. Condens. Matter* **2010**, *22*, 465804.
[19] P. J. Klar, H. Grüning, W. Heimbrodt, J. Koch, F. Höhnsdorf, W. Stolz, P. M. A. Vicente, J. Camassel, *Appl. Phys. Lett.* **2000**, *76*, 3439.
[20] B. A. Weinstein, S. R. Stambach, T. M. Ritter, J. O. Maclean, D. J. Wallis, *Phys. Rev. B* **2003**, *68*, 35336.
[21] P. R. C. Kent, Alex Zunger, *Appl. Phys. Lett.* **2003**, *82*, 559.
[22] W. J. Wang, F. H. Su, K. Ding, G. H. Li, S. F. Yoon, W. J. Fan, S. Wicaksono, B. S. Ma, *Phys. Rev. B* **2006**, *74*, 195201.
[23] G. Pettinari, A. Polimeni, F. Masia, R. Trotta, M. Felici, M. Capizzi, T. Niebling, W. Stolz, P. J. Klar, *Phys. Rev. Lett.* **2007**, *98*, 146402.
[24] J. Endicott, A. Patanè, D. Maude, L. Eaves, M. Hopkinson, G. Hill, *Phys. Rev. B* **2005**, *72*, 041306(R).
[25] A. Polimeni, F. Masia, G. Pettinari, R. Trotta, M. Felici, M. Capizzi, A. Lindsay, E. P. O'Reilly, T. Niebling, W. Stolz, P. J. Klar, *Phys. Rev. B* **2008**, *77*, 155213.
[26] A. Polimeni, M. Capizzi, M. Geddo, M. Fischer, M. Reinhardt, A. Forchel, *Phys. Rev. B* **2001**, *63*, 195320.
[27] I. A. Buyanova, M. Izadifard, W. M. Chen, A. Polimeni, M. Capizzi, H. P. Xin, C. W. Tu, *Appl. Phys. Lett.* **2003**, *82*, 3662.
[28] I. Suemune, K. Uesugi, W. Walukiewicz, *Appl. Phys. Lett.* **2000**, *77*, 3021.
[29] X. D. Luo, Z. Y. Xu, W. K. Ge, Z. Pan, L. H. Li, Y. W. Lin, *Appl. Phys. Lett.* **2001**, *79*, 958.
[30] W. Shan, W. Walukiewicz, J. W. Ager, E. E. Haller, J. F. Geisz, D. J. Friedman, J. M. Olson, Sarah R. Kurtz, *Phys. Rev. Lett.* **1999**, *82*, 1221.
[31] H. Carrère, X. Marie, L. Lombez, T. Amand, *Appl. Phys. Lett.* **2006**, *89*, 181115.
[32] K. Volz, T. Torunski, D. Lackner, O. Rubel, W. Stolz, C. Baur, S. Mueller, F. Dimroth, A. W. Bett, *J. Sol. Energy Eng.* **2007**, *129*, 266.
[33] A. Ignatov, A. Patanè, O. Makarovsky, L. Eaves, *Appl. Phys. Lett.* **2006**, *88*, 032107.
[34] S. Spasov, G. Allison, A. Patanè, L. Eaves, M. Yu Tretyakov, A. Ignatov, M. Hopkinson, G. Hill, *Appl. Phys. Lett.* **2008**, *93*, 022111.
[35] M. Bissiri, G. Baldassarri Höger von Högersthal, A. Polimeni, V. Gaspari, F. Ranalli, M. Capizzi, A. Amore Bonapasta, F. Jiang, M. Stavola, D. Gollub, M. Fischer, M. Reinhardt, A. Forchel, *Phys. Rev. B* **2002**, *65*, 235210.
[36] A. Polimeni, G. Baldassarri Höger von Högersthal, M. Bissiri, M. Capizzi, A. Frova, M. Fischer, M. Reinhardt, A. Forchel, *Semicond. Sci. Technol.* **2002**, *17*, 797.
[37] P. J. Klar, H. Grüning, M. Güngerich, W. Heimbrodt, J. Koch, T. Torunski, W. Stolz, A. Polimeni, M. Capizzi, *Phys. Rev. B* **2003**, *67*, 121206(R).
[38] A. Polimeni, G. Baldassarri H. v. H., M. Bissiri, M. Capizzi, M. Fischer, M. Reinhardt, A. Forchel, *Phys. Rev. B* **2001**, *63*, 201304(R).
[39] G. Baldassarri, H. v. H., M. Bissiri, A. Polimeni, M. Capizzi, M. Fischer, M. Reinhardt, A. Forchel, *Appl. Phys. Lett.* **2001**, *78*, 3472.
[40] A. Polimeni, M. Bissiri, M. Felici, M. Capizzi, I. A. Buyanova, W. M. Chen, H. P. Xin, C. W. Tu, *Phys. Rev. B* **2003**, *67*, 201303(R).
[41] G. Bisognin, D. De Salvador, E. Napolitani, M. Berti, A. Polimeni, M. Capizzi, S. Rubini, F. Martelli, A. Franciosi, *J. Appl. Cryst.* **2008**, *41*, 366.
[42] M. Berti, G. Bisognin, D. De Salvador, E. Napolitani, S. Vangelista, A. Polimeni, M. Capizzi, F. Boscherini, G. Ciatto, S. Rubini, F. Martelli, A. Franciosi, *Phys. Rev. B* **2007**, *76*, 205323.
[43] A. Polimeni, G. Ciatto, L. Ortega, F. Jiang, F. Boscherini, F. Filippone, A. Amore Bonapasta, M. Stavola, M. Capizzi, *Phys. Rev. B* **2003**, *68*, 085204.
[44] G. Bisognin, D. De Salvador, A. V. Drigo, E. Napolitani, A. Sambo, M. Berti, A. Polimeni, M. Felici, M. Capizzi, M. Güngerich, P. J. Klar, G. Bais, F. Jabeen, M. Piccin, S. Rubini, F. Martelli, A. Franciosi, *Appl. Phys. Lett.* **2006**, *89*, 061904.
[45] G. Ciatto, H. Renevier, M. G. Proietti, A. Polimeni, M. Capizzi, S. Mobilio, F. Boscherini, *Phys. Rev. B* **2005**, *72*, 085322.
[46] M. Felici, R. Trotta, F. Masia, A. Polimeni, A. Miriametro, M. Capizzi, P. J. Klar, W. Stolz, *Phys. Rev. B* **2006**, *74*, 085203.
[47] R. Trotta, A. Polimeni, M. Capizzi, D. Giubertoni, M. Bersani, G. Bisognin, M. Berti, S. Rubini, F. Martelli, L. Mariucci, M. Francardi, A. Gerardino, *Appl. Phys. Lett.* **2008**, *92*, 221901.
[48] F. Jiang, M. Stavola, M. Capizzi, A. Polimeni, A. A. Bonapasta, F. Filippone, *Phys. Rev. B* **2004**, *69*, 041309.
[49] Rinaldo Trotta, Antonio Polimeni, Faustino Martelli, Giorgio Pettinari, Mario Capizzi, Laura Felisari, Silvia Rubini, Marco Francardi, Annamaria Gerardino, Peter C. M. Christianen, Jan C. Maan, *Adv. Mater.* **2011**, *23*, 2706.
[50] R. Trotta, D. Giubertoni, A. Polimeni, M. Bersani, M. Capizzi, F. Martelli, S. Rubini, G. Bisognin, M. Berti, *Phys. Rev. B* **2009**, *80*, 195206.
[51] R. Trotta, A. Polimeni, M. Capizzi, F. Martelli, S. Rubini, M. Francardi, A. Gerardino, L. Mariucci, *Appl. Phys. Lett.* **2009**, *94*, 261905.
[52] T. Benabbas, Y. Androussi, A. Lefebvre, *J. Appl. Phys.* **1999**, *86*, 1945.
[53] P. Dixon, D. Richardson, R. Jones, C. D. Latham, S. Öberg, V. J. B. Torres, P. Briddon, *Phys. Status Solidi B* **1998**, *210*, 321.
[54] A. Janotti, S.B. Zhang, S.-H. Wei, *Phys. Rev. Lett.* **2002**, *88*, 125506.
[55] Y.-S. Kim, K. J. Chang, *Phys. Rev. B* **2002**, *66*, 073313.
[56] A. Janotti, S.B. Zhang, S.-H. Wei, C. G. Van de Walle, *Phys. Rev. Lett.* **2002**, *89*, 086403.
[57] A. Amore Bonapasta, F. Filippone, P. Giannozzi, M. Capizzi, A. Polimeni, *Phys. Rev. Lett.* **2002**, *89*, 216401.
[58] A. Amore Bonapasta, F. Filippone, P. Giannozzi, *Phys. Rev. B* **2003**, *68*, 115202.

[59] S. Kleekajai, F. Jiang, K. Colon, M. Stavola, W. B. Fowler, K. R. Martin, A. Polimeni, M. Capizzi, Y. G. Hong, H. P. Xin, C. W. Tu, G. Gais, S. Rubini, F. Martelli, *Phys. Rev. B* **2008**, *77*, 085213.
[60] W. B. Fowler, K. R. Martin, K. Washer, M. Stavola, *Phys. Rev. B* **2005**, *72*, 035208.
[61] M.-H. Du, S. Limpijumnong, S. B. Zhang, *Phys. Rev. B* **2005**, *72*, 073202.
[62] G. Ciatto, F. Boscherini, A. Amore Bonapasta, F. Filippone, A. Polimeni, M. Capizzi, *Phys. Rev. B* **2005**, *71*, 201301(R).
[63] A. Amore Bonapasta, F. Filippone, G. Mattioli, *Phys. Rev. Lett.* **2007**, *98*, 206403.
[64] L. Wen, F. Bekisli, M. Stavola, W. B. Fowler, R. Trotta, A. Polimeni, M. Capizzi, S. Rubini, F. Martelli, *Phys. Rev. B***2010**, *81*, 233201
[65] M. Geddo, T. Ciabattoni, G. Guizzetti, M. Galli, M. Patrini, A. Polimeni, R. Trotta, M. Capizzi, G. Bais, M. Piccini, S. Rubini, F. Martelli, A. Franciosi, *Appl. Phys. Lett.* **2007**, *90*, 091907.
[66] J. Alvarez, J. P. Kleider, R. Trotta, A. Polimeni, M. Capizzi, F. Martelli, L. Mariucci, S. Rubini, *Phys. Rev. B* **2011**, *64*, 085331.
[67] R. A. Morrow, *J. Appl. Phys.* **1989**, *66*, 2973.
[68] D. Granados, J. M. García, T. Ben, S. I. Molina, *Appl. Phys. Lett* **2005**, *86*, 071918.
[69] M. Felici, A. Polimeni, G. Salviati, L. Lazzarini, N. Armani, F. Masia, M. Capizzi, F. Martelli, M. Lazzarino, G. Bais, M. Piccin, S. Rubini, A. Franciosi, *Adv. Mater.* **2006**, *18*, 1993.
[70] L. Felisari, V. Grillo, F. Martelli, R. Trotta, A. Polimeni, M. Capizzi, F. Jabeen, L. Mariucci, *Appl. Phys. Lett.* **2008**, *93*, 102116.
[71] T. Taliercio, R. Intartaglia, B. Gil, P. Lefebvre, T. Bretagnon, U. Tisch, E. Finkman, J. Salzman, M.-A. Pinault, M. Laügt, E. Tournié, *Phys. Rev. B* **2004**, *69*, 073303.
[72] R. Trotta, L. Cavigli, L. Felisari, A. Polimeni, A. Vinattieri, M. Gurioli, M. Capizzi, F. Martelli, S. Rubini, L. Mariucci, M. Francardi, A. Gerardino, *Phys. Rev. B* **2010**, *81*, 235327.
[73] V. Zwiller, M.-E. Pistol, D. Hessman, R. Cederström, W. Seifert, L. Samuelson, *Phys. Rev. B* **1999**, *59*, 5021.
[74] P. Castrillo, D. Hessman, M.-E. Pistol, N. Carlsson, L. Samuelson, *Appl. Phys. Lett.* **1995**, *67*, 1905.
[75] X. Wang, X. Ren, K. Kahen, M. A. Hahn, M. Rajeswaran, S. Maccagnano-Zacher, J. Silcox, G. E. Cragg, A. L. Efros, T. D. Krauss, *Nature* **2009**, *459*, 686.
[76] Ch. Gréus, L. Butov, F. Daminger, A. Forchel, P. A. Knipp, T. L. Reinecke, *Phys. Rev. B* **1993**, *47*, 7626(R).
[77] N. Panev, A. I. Persson, N. Sköld, L. Samuelson, *Appl. Phys. Lett.* **2003**, *83*, 2238.
[78] P. Senellart, E. Peter, J. Hours, A. Cavanna, J. Bloch, *Phys. Rev. B* **2005**, *72*, 153021.
[79] H. Htoon, A. V. Malko, D. Bussian, J. Vela, Y. Chen, J. A. Hollingsworth, V. I. Klimov, *Nano Lett.* **2010**, *10*, 2401.
[80] S. N. Walck, T. L. Reinecke, *Phys. Rev. B* **1998**, *57*, 9088.
[81] M. Abbarchi, T. Kuroda, T. Mano, K. Sakoda, M. Gurioli, *Phys. Rev. B* **2010**, *81*, 035334.
[82] A. Mohan, M. Felici, P. Gallo, B. Dwir, A. Rudra, J. Faist, E. Kapon, *Nat. Photonics* **2010**, *4*, 302.
[83] J. Stangl, V. Holý, G. Bauer, *Rev. Mod. Phys.* **2004**, *76*, 725.
[84] S. A. Blanton, M. A. Hines, P. Guyot-Sionnest, *Appl. Phys. Lett.* **1996**, *69*, 3905.
[85] G. Bastard, *Wave Mechanics Applied to Semiconductor Heterostructures*, Les Editions de Physique, Les Ulis, France **1988**.
[86] F. H. Pollak, M. Cardona, *Phys. Rev.* **1968**, *172*, 816.
[87] Suwit Kiravittaya, Armando Rastelli, Oliver G Schmidt, *Rep. Prog. Phys.* **2009**, *72*, 046502.
[88] M. Notomi, J. Hammersberg, H. Weman, S. Nojima, H. Sugiura, M. Okamoto, T. Tamamura, M. Potemski, *Phys. Rev. B* **1995**, *52*, 11147.
[89] F. Vouilloz, D. Y. Oberli, M.-A. Dupertuis, A. Gustafsson, F. Reinhardt, E. Kapon, *Phys. Rev. Lett.* **1997**, *78*, 1580.
[90] S. Francoeur, J. F. Klem, A. Mascarenhas, *Phys. Rev. Lett.* **2004**, *93*, 067403.
[91] K. Rammohan, Y. Tang, D. H. Rich, R. S. Goldman, H. H. Wieder, K. L. Kavanagh, *Phys. Rev. B* **1995**, *51*, 5033.
[92] J. P. van der Ziel, Naresh Chand, J. S. Weiner, *J. Appl. Phys* **1989**, *66*, 1195.
[93] R. Swanepoel, *J. Phys. E: Sci. Instrum.* **1983**, *16*, 1214.
[94] G. Ghosh, *Handbook of thermo-optic coefficients of optical materials with applications*, Academic Press, San Diego, CA **1998**.
[95] S. Zollner, *Appl. Phys. Lett.* **1993**, *63*, 2523.
[96] S. Adachi, *Optical constants of crystalline and amorphous semiconductors*, Kluwer Academic Publisher, Boston, MA **1999**.
[97] P. Bhattacharya, *Semiconductor optoelectronic devices*, Prentice Hall, Englewood Cliffs, NJ **1997**.
[98] M. Geddo, M. Patrini, G. Guizzetti, M. Galli, R. Trotta, A. Polimeni, M. Capizzi, F. Martelli, S. Rubini, *J. Appl. Phys.* **2011**, *109*, 123511.
[99] Ryan O'Hayre, Minhwan Lee, Fritz B. Prinz, *J. Appl. Phys.* **2004**, *95*, 8382.
[100] J. Alvarez, F. Houzé, J. P. Kleider, M. Y. Liao, Y. Koide, *Superlattices Microstruct.* **2006**, *40*, 343.
[101] P. Eyben, W. Vandervorst, D. Alvarez, M. Xu, M. Fouchier, in *Scanning Probe Microscopy*, vol. I (Eds: S. Kalinin, A. Gruverman), Springer, New York **2007**, Ch. 1, p. 31.
[102] D. Haberer, D. V. Vyalikh, S. Taioli, B. Dora, M. Farjam, J. Fink, D. Marchenko, T. Pichler, K. Ziegler, S. Simonucci, M. S. Dresselhaus, M. Knupfer, B. Buchner, A. Gruneis, *Nano Lett.* **2010**, *10*, 3360.
[103] R. Farshchi, O. D. Dubon, D. J. Hwang, N. Misra, C. P. Grigoropoulos, P. D. Ashby, *Appl. Phys. Lett.* **2008**, *92*, 012517.